Rod Coating MoS_2 Films and Silver Nanowire Electrodes for 2D Material-based Devices

by

Zhiqiao Yang

A thesis
presented to the University of Waterloo
in fulfillment of the
thesis requirement for the degree of
Master of Applied Science
in
Electrical and Computer Engineering

Waterloo, Ontario, Canada, 2023

Author's Declaration

I hereby declare that I am the sole author of this thesis. This is a true copy of the thesis, including any required final revisions, as accepted by my examiners.

I understand that my thesis may be made electronically available to the public.

Abstract

Two dimensional materials have become a research area under intensive investigation as quantum confinement within the material structure results in unique electrical and optical properties, making them a promising candidate for next-generation electronic and optoelectronic devices. Among these materials, molybdenum disulfide (MoS_2), belonging to a class of materials known as transition metal dichalcogenides, is a semiconductor with a layer-dependent bandgap, strong light-matter interaction, and potentially high in-plane carrier mobility. There have been studies on the applications of MoS_2 in thin film transistors (TFTs) [1,2], photodetectors [3,4] and chemical sensors [5,6] featuring proof-of-concept devices based on MoS_2 prepared by mechanical exfoliation or bottom-up synthesis. The development of dispersions of MoS_2 flakes through solution-processing exfoliation methods presents an opportunity to produce large-scale thin films of MoS_2. Mayer rod coating is a convenient method to deposit dispersions of materials over a large area on a variety of substrates. In contrast to other common solution processing deposition methods for the assembly of 2D materials reported in the literature, such as vacuum filtration which requires a transfer process, a time-consuming Langmuir-Blodgett method, and spin coating which prepares thin films with a limited thickness, rod coating distinguishes itself through its simplicity, versatility and scalability, presenting an alternative approach to prepare solution-processed thin films of 2D materials.

To the best knowledge of the author, it is the first time Mayer rod coating was applied to deposit thin films of solution-processed MoS_2. Five experimental parameters including the concentration of MoS_2 flakes in the dispersion, wire diameter of Mayer rod (rod number), number of coats, hydrophilicity/hydrophobicity of the substrate and thermal annealing temperature, are found to influence the morphological and electrical property of the fabricated film. Mayer rod

coating is demonstrated to be a feasible approach for assembling 2D materials in a scalable manner, suitable for roll-to-roll production in the industry. Still, uniformity is one major limitation of the rod-coated film. An optimized rod-coated MoS_2 film with continuous coverage of MoS_2 flakes at a micron scale on the substrate is achieved by rod coating 100 mg/ml MoS_2 dispersion for 16 coats on SiO_2/Si substrates treated by piranha solution and oxygen plasma. Different thermal annealing temperatures between 100 ˚C and 400 ˚C were investigated, and the sheet resistance of rod-coated MoS_2 film experienced a dramatic reduction to the order of kΩ/□ after annealed at 400 ˚C in argon for 30 minutes. Subsequent integration of the optimal rod-coated MoS_2 film into thin film transistors reveals non-linear s-shaped $I_{sd} - V_{sd}$ characteristics, probably due to inter-flake junction resistance in the MoS_2 flake film. On the other hand, there is no significant gate modulation effect observed in electrical characterization, which can be attributed to defects in the solution-processed MoS_2 film, adsorbates on the dielectric interface and the large thickness of MoS_2 film.

Rod coating is also employed for the deposition of silver nanowires, an indication of its versatility in film assembly of 2D and low-dimensional materials. Silver nanowires were incorporated as a transparent electrode in light emitting devices (LEDs) based on WS_2, fulfilling the function of transparent LED evidenced by its bidirectional emission with comparable luminance. LEDs featuring an emissive area of several mm^2 exhibited an average transmittance exceeding 60% in the visible spectral range. Among the fabricated devices, the one with the most outstanding performance demonstrated a turn-on voltage of around 3 V and a luminance of 8.8×10^{-2} cd/m^2. However, it is worth noting that its external quantum efficiency remained relatively low, measuring on the order of 10^{-5} %. In spite of the reasonable luminance yielded by the device, the long-term durability and a random distribution of silver nanowires were constraints to the performance of silver nanowire electrodes.

Acknowledgements

First and foremost, I would like to express my deep gratitude to my supervisors, Professor Irene Goldthorpe and Professor Na Young Kim, for their unwavering support and invaluable guidance throughout this study. They not only provided insightful advice to help me overcome obstacles I encountered in the research but also set an example of dedication to rigorous scholarship, inspiring me to improve my abilities to conduct scientific research.

I would like to thank Nathan Nelson-Flizpatrick, Lino Eugene, Greg Holloway, Sandra Gibson, Matt Scott, Rod Salandanan and Ken Speirs at the Quantum-Nano Fabrication and Characterization Facility (QNFCF) for their training on equipment. I am particularly appreciative of Lino Eugene and Greg Holloway for sharing their fields of expertise with me and offering suggestions to improve my device fabrication process and navigate challenges encountered along the way.

My gratitude also extends to the members of Goldthorpe's group, including Dr. Jon Atkinson, Muhammed Kayaharman and Tiancheng Xu as well as Heebong Yang in Kim's group for their thoughtful suggestions, assistance, and constant support throughout my master's program.

Table of Contents

List of Figures

List of Tables

Chapter 1 Introduction

1.1 Two Dimensional Materials

1.1.1 Categories of 2D materials

Two-dimensional (2D) materials are a class of materials that consist of single-layered structures with atomic thickness. The reduced dimensionality of these materials often gives rise to unique properties that differ from their bulk counterparts. They can be derived from their bulk parent materials and be manipulated into thin layers using various techniques. The pioneering discovery of 2D material was made in 2004 by Novoselov, Geim et al., who successfully exfoliated graphene using scotch tape [7]. Graphene is comprised of a single layer of carbon atoms bonded by covalent bonds, forming a honeycomb lattice structure. Adjacent layers interact through van der Waals force. The significant difference in mechanical strength between chemical bonds and van der Waals force allows the isolation of graphene from graphite via shear in-plane force without compromising the structural integrity of the planar sheets. Graphene possesses several remarkable properties including high carrier mobility, large optical transparency due to its atomic thickness, excellent thermal conductivity, and a high Young's modulus.

Since then, more and more 2D materials have been discovered and investigated by the scientific community. Hexagonal boron nitride (h-BN) shares a similar chemical structure with graphene, except that one boron and one nitrogen atom constitute the honeycomb lattice's two-atom basis. Hence, it is also known as 'white graphene.' In contrast to graphene as a semimetal, h-BN is an electrically insulating material with a wide bandgap of 6 eV. Transition metal dichalcogenides (TMDs) (MX_2, where M = Mo, Bi, Ta, V, Ti, Nb, W, Hf, Zr and X= S, Se, Te) are a class of materials which have also been extensively studied. Currently, there are over 40

different compounds reported in the literature belonging to this class of material. Transition atoms in TMDs reside at the center of octahedrons or trigonal prisms of chalcogen atoms, constituting the 1T and 2H phases, respectively. TMDs can either be semiconducting, with layer-dependent bandgaps, such as MoS_2, WS_2 and $MoTe_2$, or metallic, like $NbSe_2$ and TiS_2, because of the coordination and oxidation state of transition metals and chemical structures [11]. Black phosphorus (BP) is another intriguing 2D material that has captured the interest of the research community. Unlike TMDs, which exist naturally, BP is synthesized from other allotropes of phosphorus (red or white phosphorus) to form an orthorhombic pleated honeycomb structure. Similar to graphene, the interlayer interaction of h-BN, TMDs and BP is through van der Waals force. Therefore, these materials fall into the same category, often collectively referred to as Van der Waals materials. The weak van der Waals force enables the exfoliation of these materials from their bulk parent materials, either through mechanical exfoliation or liquid phase exfoliation [8,9].

Various types of layered materials fall under the category of 2D materials. Layered ionic compounds, for instance, consist of a charged polyhedral layer held between hydroxide or halide layers by electrostatic forces [10]. A single or a few layers of these materials can be exfoliated by ion intercalation or the ion exchange exfoliation method. During the exfoliation process, the adsorption of foreign molecules and the replacement of parent ions with heavier ions lead to an increase in the spacing of basal planes and a weakening of the interlayer bonding of basal planes [10]. Peroxide-type oxides (eg. $LaNb_2O_7$, $Bi_4Ti_3O_{12}$, $Ca_2Ta_2TiO_{10}$, etc.) and metal hydroxides (e.g. Eu $(OH)_2$, $Co_{2/3}Fe_{1/3}(OH)_2^{1/3+}$, etc.) are examples of this category of materials. Another type of 2D material is surface-assisted nonlayered solids, which are synthesized on a substrate through chemical vapour deposition and epitaxial growth [10]. One prominent example is silicene, which shares similarities with graphene but is composed of silicon atoms arranged in a honeycomb lattice.

Contrary to graphene, silicene is unstable under ambient conditions, restricting its potential applications in electronic and optoelectronic devices [10]. An intriguing class of 2D materials currently under active research is Mxenes, atomically thin layers of transition metal carbide, nitride, and carbonitride. They are obtained by selectively etching metal atoms in layered ternary carbides and nitrides known as MAX phases and subsequent exfoliation. Theoretical studies have suggested that Mxenes can be either metallic or semiconductors with small bandgaps that could be manipulated through chemical functionalization [11-14].

1.1.2 Applications of 2D materials

The preceding discussion has showcased the diversity of 2D materials and the broad range of their physical properties. The unique characteristics of 2D materials arise from their atomically thin nature, which induces a quantum confinement effect, leading to significant performance enhancements and even exotic properties not observed in their bulk counterparts. One important consequence of the quantum confinement effect is a pronounced change in the density of states. Qualitatively, the density of states of 2D materials is expected to exhibit a quasi-continuous step-like increase with energy [10]. The difference in the density of states between 2D materials and bulk materials are attributed to the distinctive electrical properties of 2D materials, holding potential for applications in next-generation high-performance electronics and optoelectronics. Different 2D materials offer a wide range of bandgap values, encompassing metallic materials such as graphene and certain Mxenes and TMDs, semiconductors like BP and TMDs, and insulating materials with a large bandgap like h-BN. In view of the high optical transparency and great electrical conductivity of graphene, it is an ideal candidate for transparent electrodes in flexible electronics and optoelectronics. TMDs and BP, with layer-dependent band gaps, can serve as semiconductor channels in field effect transistors (FETs). Monolayer or a few layers of TMDs and BP with direct

bandgaps show great promise as light-sensing and light-illuminating materials in photodetectors and light-emitting devices [11,29,39,76]. The integration of these materials with other 2D materials or quantum dots to form heterojunctions opens up the possibility of fabricating broad- band photodetectors based on low-dimensional materials. And these materials are mechanically flexible, useable for bendable or foldable devices. This represents an improvement over photodetectors based on conventional semiconductors (eg. Silicon, III-V semiconductor), which typically have a specific spectral response range limited by their bandgaps and are rigid. And some of them need to operate at low temperatures. These problems could be addressed by the application of semiconducting 2D materials. Moreover, insulating h-BN with an atomically smooth surface and the absence of dangling bonds is an ideal dielectric layer in devices based on heterojunctions of other 2D materials [15-17]. It is important to note the applications of 2D materials are not limited to electronics and optoelectronics. For instance, the high mechanical strength of graphene makes it a suitable filler material. Similarly, exfoliated h-BN, with remarkable dielectric and thermal properties, can function as a filler material for polymer composite [18]. In addition, 2D materials have substantial interaction with chemical molecules such as NH_3 and NO_2, and biomolecules like DNA due to the large specific surface area, making them valuable for applications in biological or chemical sensors [11,19,39]. Moreover, Mxenes show great promise in energy storage devices, such as supercapacitors and batteries, owing to their electrochemical properties [20]. Thus overall, 2D materials have an immense scientific and commercial interest.

1.2 Deposition Methods of Solution-Processed 2D Material

1.2.1 Preparation of 2D materials

The initial stage in harnessing the potential of 2D materials involves material preparation, laying the foundation for subsequent applications. Two strategies to prepare 2D materials are

bottom-up synthesis and top-down exfoliation. In the context of bottom-up synthesis, chemical vapour deposition (CVD) [21,22] is a widely used method in which gaseous precursor molecules are introduced into a reaction chamber and subsequently undergo reactions on the surface of a heated substrate to form a thin film of high-quality 2D materials in a controlled manner through parameters such as temperature, pressure, precursor flow rate and deposition time. The selection of substrate also wields a considerable influence over the growth process and properties of the deposited materials. At times, circumstances necessitate transferring CVD-grown 2D materials onto designated target substrates, a process that is complex and can potentially introduce defects into the material structure. Beyond CVD, several other methods have been utilized to synthesize 2D materials. Atomic layer deposition (ALD) [23] operates through the sequential exposure of the substrate to precursor gases, allowing for the deposition of a single atomic layer in each cycle because of the self-limiting growth mechanism. In molecular beam epitaxy (MBE) [24-26], source materials are heated in effusion cells to produce a flux of vaporized species. The resulting molecular beams of vaporized species are directed toward the substrate surface in an ultra-high vacuum environment to achieve layer-by-layer growth. Despite the excellent control ALD and MBE provide over film thickness and composition, ALD is limited by its slow deposition process, and MBE is constrained by the requirement of an ultra-high vacuum environment coupled with a complex operational procedure. Pulsed magnetron sputtering [27,28] is a variation of conventional magnetron sputtering, in which alternating cycles of high-density and low-density plasma bombard the target material so that dislodged atoms from the target deposit onto the substrate. While pulse magnetron sputtering allows for a relatively high deposition rate, it lacks precise control over film thickness at the atomic scale compared to ALD and MBE. It may introduce defects into the material as well due to ion bombardment. Bottom-up synthesis methods, while capable of

producing high-quality films of 2D materials, the fabrication process can be complex and usually requires elevated temperature and high vacuum conditions. A subsequent process may be involved to transfer the synthesized film to a designated substrate. Scaling up the process for the fabrication of large-area uniform films also presents a challenge.

Top-down methods exfoliate monolayer or few-layer 2D materials from bulk or layered materials by overcoming the relatively weak inter-layer interaction with applied forces such as sonication, shear force, and ball milling. Top-down methods can be broadly categorized into two approaches: mechanical exfoliation and solution processing exfoliation. Mechanical exfoliation was initially adopted to isolate graphene from graphite with simple scotch tape. Although mechanical exfoliation offers a simple and fast process, its drawbacks lie in the extremely low yield of monolayer materials and lack of scalability [10]. In contrast, there are several advantages of solution processing exfoliation, including the potential for large-scale production of 2D materials at low cost, solution processability of exfoliated materials and versatility [29]. Unlike top-down methods, bottom-up synthesis methods depend on the specific type of 2D material, owing to differences in chemical compositions. Solution processing exfoliation methods include liquid phase exfoliation and ion intercalation/exchange exfoliation. In the case of graphene, there is an alternative and commonly utilized approach to produce reduced graphene oxide through the reduction of graphene oxide [30]. In ultrasound-assisted liquid phase exfoliation, bulk layered materials dispersed in a suitable solvent were subject to ultrasonication [8, 31-32]. Ultrasonic waves create cavitation bubbles in the solvent, and the subsequent collapse of bubbles generates intense shear forces to weaken the interlayer interactions, facilitating the exfoliation of 2D material flakes. Besides ultrasonication, other frequently employed methods to generate shear force are high-shear mixing, high-pressure mixing, and ball milling [11, 33-35]. The selection of solvent with a surface

tension that resembles the surface energy of layered 2D materials serves dual purposes, reducing the energetic cost of exfoliation and preventing the re-agglomeration of nanosheets [10]. N-methyl-2-pyrrolidone (NMP), dimethylformamide (DMF), isopropyl alcohol (IPA) and N-vinylpyrrolidone (NVP) are among the common solvents for liquid phase exfoliation [8,36-38]. The high boiling point of some organic solvents is not desirable for processing and deposition of the dispersion, so there has been the utilization of surfactants (ionic: amphiphile; non-ionic: Triton-X, Tween and Brij series) and polymers (e.g. sodium carboxymethylcellulose (Na-CMC), polyvinylpyrrolidone (PVP), ethyl cellulose) in combination with low-boiling point solvents to provide electrostatic or steric stabilization in 2D material dispersions [11]. Regarding the ion intercalation process, ionic species such as alkali metal ions or organic ions intercalate between layers of bulk materials, leading to an increase in interlayer spacing that weakens the interlayer interactions, thereby facilitating the separation of the layers. On the other hand, ionic species intercalate and exchange with ions present in layered materials in the ion exchange process via charge transfer and weakening of interlayer interactions. Through mild sonication or shear mixing, separated nanosheets of 2D materials are exfoliated into monolayers or a few layers. In comparison with liquid phase exfoliation, ion intercalation or exchange exfoliation can produce flakes with a narrower distribution of thickness, a larger lateral size and improved quality. However, the process of liquid phase exfoliation is more straightforward and suitable for a wide range of materials. Following solution processing exfoliation, flakes with heterogeneous dimensions in the dispersion are sorted by centrifugation. Isopycnic density gradient ultracentrifugation allows the precise thickness separation of 2D material flakes according to buoyant density [10, 11].

The lateral size and thickness of flakes or nanosheets prepared by solution processing exfoliation methods are dependent on the specific material, exfoliation method and processing

conditions. Generally, liquid phase exfoliation can yield 2D materials with a thickness ranging from monolayer to tens of layers and lateral size of about several hundred nanometers, while ion intercalation/exchange exfoliation produces 2D materials with a narrower distribution in thickness (monolayer to few layers) and a larger lateral size on the order of microns [39]. Although the quality of 2D materials prepared by solution processing exfoliation may not match those obtained through mechanical exfoliation or bottom-up synthesis, it is able to produce a large quantity of 2D materials at a low cost and is compatible with solution deposition methods. For applications that require expansive 2D films, sorted flakes can be redispersed in a different solvent or utilized directly in their initial solvent to formulate dispersions, subsequently deposited using solution deposition methods. In contrast to the bottom-up synthesis methods, solution deposition methods are generally simpler in their operations and less demanding of the deposition conditions. Although the quality of films fabricated by solution processing methods may be inferior to bottom-up synthesis, solution processing methods are well-suited for depositing thin films over a large area at a low cost, making them ideal for applications such as flexible electronics and sensors. Solution deposition can generally deposit materials on any substrate including plastics and even textiles. The formation of heterostructures, which can lead to highly desirable functions, is also much easier as bottom-up synthesis is very dependent on the substrate or underlying layer. Seven common solution-processing deposition methods are briefly described and compared in the following paragraphs as well as summarized in Table 1.1.

1.2.2 Layer-by-layer Assembly

Layer-by-layer assembly [40-42], a method founded on electrostatic deposition, serves to assemble films of charged 2D material. The substrate is sequentially immersed into an aqueous solution of oppositely charged polyelectrolyte and a dispersion of 2D materials is adsorbed onto

substrates with opposite charges through electrostatic interactions. Dispersions utilized for this process are diluted to achieve a satisfying stability of charged 2D materials, with a concentration lower than 0.1 g/L [29,39]. This method involves a straightforward operation procedure and can be easily scaled up to deposit a film over a large area. Its versatility renders it a frequently employed approach for the assembly of not only 2D materials but also other low-dimensional materials. Another benefit of this method is its capability to deposit 2D materials with a thickness as minuscule as a monolayer (~ 1nm) in each deposition cycle. Nonetheless, the fabrication process can be time-consuming. There is a limitation to the film thickness, typically not exceeding 50 nm due to the increasing roughness of the film surface during deposition.

1.2.3 Electrophoretic Deposition

Electrophoretic deposition (EPD) [43-46] relies on electrophoresis, a phenomenon where charged materials in a dispersion migrate toward an oppositely charged electrode when subjected to an electric field. Given the commonly charged nature of solution-processed 2D materials, EPD is a viable method [29]. A stable suspension of 2D materials is a prerequisite for a successful EPD process. By immersing a conductive substrate as the cathode and a contour electrode as the anode in the suspension, 2D materials with lateral size below 50 μm can be driven toward the electrode with opposite charges under the influence of an applied electric field, leading to their deposition on the substrate. The resulting film thickness and uniformity are controlled by electric field strength, deposition time and properties of dispersion (e.g. concentration, pH). The appeal of EPD lies in its simple and low-cost equipment setup, and its ability to assemble large-scale thick films on the substrates. Via manipulation of current during the EPD process, the deposition of films with various morphologies, such as free-standing film, winkle film and multi-layer 2D composites, can be achieved [29]. This method can also be utilized to fabricate heterostructures or patterned

structures of 2D materials. It should be aware that potential chemical reactions like reduction or aqueous electrolysis during the EPD process could induce side effects impacting the assembled film [29, 44].

1.2.4 Langmuir-Blodgett Assembly

Langmuir-Blodgett assembly has emerged as a method for fabricating well-structured thin films of 2D materials [47-52]. The dispersion of 2D materials is spread onto the surface of a liquid subphase inside a trough, forming a monolayer of 2D materials at the air-liquid interface as a consequence of their hydrophilic or hydrophobic interactions with the solvent. The floating film is compressed with a pair of movable barriers to increase the surface pressure and result in the packing of 2D materials into a well-organized monolayer. A substrate possessing good affinity with the liquid is slowly dipped into the liquid subphase covered by a monolayer of 2D materials and subsequently lifted out of the subphase at a controlled speed to deposit a monolayer of 2D materials on the substrate. Multiple layers of 2D materials can be deposited on the substrate by repeating the process. Langmuir-Blodgett method provides precise control of film thickness and produces high-quality thin films of densely packed 2D materials with alignment. It also allows the fabrication of heterostructures of 2D materials with stacking layer structure. Yet there still are some drawbacks to this method. It is time-consuming, and the size of the prepared film is small.

1.2.5 Spin Coating

Spin coating [53-56] is a common method to prepare thin films in the semiconductor industry. A certain amount of 2D materials in solution is dropped onto a substrate, which is then rotated at a suitable speed to spread the dispersion evenly across its surface. Excess solvent and material are thrown off the edges of the substrate due to centrifugal force generated by substrate spinning. Solvent evaporation in the spinning process leaves a thin and uniform layer of 2D materials on the

substrate. Subsequent UV treatment or thermal annealing could be performed to improve the film adhesion to the substrate. The thickness of the spin-coated film is determined by several factors, including solution concentration, dispersion viscosity and spin speed. Films with multiple layers can be obtained by repeating the process. Spin coating offers a simple and fast approach to depositing thin films with controlled thickness. On the other hand, spin coating is not suitable for preparing films with thickness exceeding 50 nm, as achieving a uniform thick film using spin coating method becomes challenging and would involve complicated cycling process and dispersion formulations [29,39]. Spin coating is also not scalable to large areas.

1.2.6 Vacuum Filtration

Vacuum filtration [57,58] is another widely used method to deposit thin films of 2D materials. The dispersion of 2D materials is filtered through a porous membrane (composed of materials like polytetrafluoroethylene or cellulose), driven by the pressure difference generated by a vacuum pump on opposite sides of the filter membrane. Solvent and flakes with a size smaller than pores pass through the membrane, leaving a film of 2D materials on top of the membrane. The resulting film thickness typically falls within the range of 1.8 nm to 100 μm, which can be adjusted based on the pore size of the filter membrane and the amount of 2D material flakes in the dispersion [39, 59]. Vacuum filtration provides a simple and fast process to prepare films of 2D materials using a cost-effective setup. It can fabricate a relatively thick film easily compared to other methods and yield free-standing films after their release from the membrane. However, it could be time-consuming to prepare a film with a thickness of several hundred micrometres due to a pronounced blocking effect when the film is thicker than 100 μm [29, 39]. In addition, thin films with a thickness lower than 20 nm [29] need an additional process to be transferred onto a target substrate, which undermines the competitiveness of vacuum filtration in preparing high-quality thin films.

1.2.7 Inkjet Printing

Inkjet printing [60-63] is a promising method to prepare pre-patterned thin films of 2D materials for applications in electronic and optoelectronic devices. Similar to conventional inkjet printing, the evaporation of a portion of ink by thermal heating or a piezoelectric element applied with an electric pulse generates pressure on the ink reservoir, and droplets of 2D material ink are ejected out of the nozzle and onto the substrate in a controlled manner. Successful printing requires the optimization of ink formulations to produce patterns with densely stacked flakes and sharp edges in high resolution. Substantial efforts have been devoted to enhancing the properties of the solvent and selecting the suitable surfactant for developing stable, well-dispersed and concentrated inks of 2D materials. An ideal solvent for ink formulation should be able to disperse high concentrations of 2D materials efficiently while being cost-effective and non-toxic. Solvents with high boiling points are commonly used for suspensions of 2D materials. However, there are concerns over the degradation of the resulting film performance caused by the residue of solvents with high boiling points and their toxicity. Alternative solvents with low boiling points and efficient dispersion properties are employed for printing to circumvent these issues, such as terpineol and a pyrene sulfonic acid water solution [64,65]. Inkjet printing can directly print 2D materials in complicated patterns with a good spatial resolution of around 5 μm. It also minimizes the waste of materials as the ink is only deposited in selected areas. Moreover, this method is suitable for most 2D materials and compatible with a wide range of substrates. Nonetheless, disorder exists in the structure of inkjet-printed 2D materials, influencing the performance of devices and limiting their applications in scenarios that demand alignment [29].

1.2.8 Spray Coating

Spray coating [66-68] is another method to deposit solution-processed films in an area-selective manner. Aerosol droplets of 2D material dispersions generated by gas pressure or electric voltage are propelled onto a substrate, resulting in the deposition of a thin film as the solvent evaporates due to the large specific surface area of droplets. It is simple to deposit 2D materials over a large area on a variety of substrates (e.g. glass, silicon, flexible substrates) at a low cost using spray coating. Through the use of a shadow mask, spray coating can also be utilized for the deposition of patterns of 2D materials with a spatial resolution of about 100 μm or smaller without patterning by photolithography. Spray coating is preferable to inkjet printing in fabricating large-area devices with a simple stacking layer structure because of its speed and cost-effectiveness. The major disadvantage of spraying coating is its need for a mask and manual replacement of the mask [39]. In contrast, inkjet printing allows for the fabrication of multilayered structures automatically without the requirement of manual procedure, which is essential for intricate device designs [39].

Table 1-1 Different methods to deposition solution-processed film. Take reference from [29] and [39].

Deposition Method	Advantages	Disadvantages
Layer-by-Layer Assembly	1. Simple 2. Control of film thickness 3. Suitable for large-area assembly	1. Time-consuming for thick films 2. 2D materials need to be charged 3. Film quality influenced by polyelectrolyte in the dispersion
Electrophoretic Deposition	1. Simple 2. Able to deposit large-area thick film	1. 2D materials need to be charged 2. Side effects from chemical reactions during the process
Langmuir-Blodgett	1. Simple 2. High controllability over film properties 3. Deposition of a thin film with high quality 4. Suitable for most 2D materials	1. Time-consuming 2. Small size of prepared film
Spin Coating	1. Simple and fast 2. Control of film thickness	1. Thickness difficult to control 2. Less suitable for large-area coating 3. Not ideal for dispersions with high viscosities

Vacuum Filtration	1. Simple and fast 2. Preparation of free-standing film 3. Suitable for most 2D materials	1. Additional transfer process is required 2. Difficult to prepare thick film 3. Not suitable for large-areas
Inkjet Printing	1. Direct writing of 2D materials with patterns 2. Good spatial resolution: ~ 5 μm 3. Suitable for most 2D materials	1. Relatively complicated and expensive printing instruments 2. Potential challenges in preparing stable and well-dispersed inks of 2D materials 3. Slow (limited throughput) 4. Cannot print larger flakes due to nozzle clogging
Spray Coating	1. Simple 2. Able to deposit over large area 3. Suitable for most 2D materials	1. Difficult to precisely control film thickness and uniformity 2. Limited film thickness 3. Spatial resolution ~ 100 μm

1.3 Rod Coating as a Thin Film Deposition Method

Despite the many solution deposition techniques that exist for assembling 2D flakes into films, as pointed out in a review paper [29], no method meets all the desired criteria for controllable, scalable, cost-effective, and high-quality flake film assembly. In this thesis, Mayer rod coating is considered as a method that could meet all these criteria. Mayer rod coating is a widely used coating technique in industry to deposit liquid film in a controlled manner [29]. A setup of the Mayer rod coating process is illustrated in Figure 1.1. This method involves the use of a Mayer rod, which is a metal bar with a wire wound around its surface. The deposition of solution-processed thin film is achieved by drawing the Mayer rod across the substrate. The thickness of the wet film is determined by the diameter of the wire. During the coating, the solution is drop-cast onto the substrate and flows through the grooves of the Mayer rod, leaving a series of stripes on the substrate with a width corresponding to the separation of the wire winding. Surface tension comes into play immediately, causing these stripes to merge and form a continuous film.

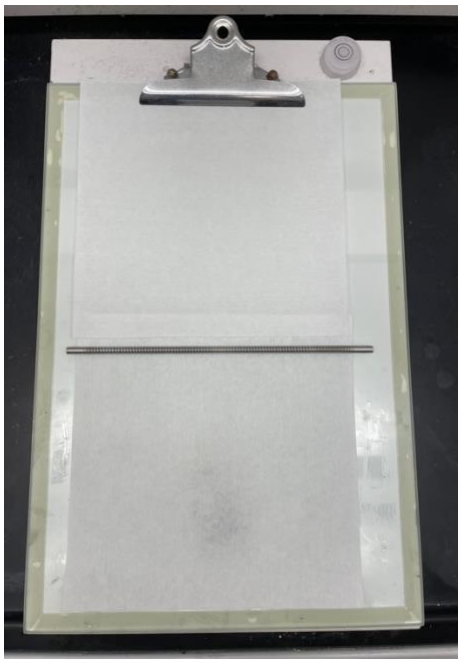

Figure 1.1 Setup of rod coating.

Mayer rod coating offers a different approach for depositing dispersions of 2D materials. This method allows the direct deposition of flakes onto various target substrates such as glass, silicon, and polyethylene terephthalate (PET) at room temperature, without the need for a transfer process as required in vacuum filtration and Langmuir Blodgett. It could deposit 2D materials over a large area in a simple, fast, and high-throughput roll-to-roll process in comparison with most of the methods summarized in the last subsection, such as time-consuming layer-by-layer assembly. Rod coating is generally suitable for most 2D materials in a stable dispersion and does not require 2D materials to be charged, as in electrophoretic deposition and layer-by-layer assembly. In contrast to inkjet printing, which demands a high-concentration ink of 2D materials, rod coating enables the deposition of a continuous film using a solution with a relatively low concentration of 2D materials. Preparing dispersions of 2D materials at a high concentration could be problematic as flakes tend to agglomerate at higher concentrations, thereby prohibiting the ability to print ultra-thin films. Rod-coating could also be used to deposit large flakes, which in inkjet printing would

clog the nozzle. When compared to spray coating, flakes deposited through rod coating probably lie flat on the substrate, leading to the formation of a thin film with a smooth surface. Unlike a thin film deposited by the Langmuir Blodgett technique, where flakes are in edge-to-edge contact, flakes deposited by rod coating are more likely to overlap. The overlap between flakes increases the contact area and thereby reduces the contact resistance.

In the literature, there have been only a few reports on rod coating as a method for depositing films of 2D flakes. Previous research on this technique has primarily focused on graphene [69-72] and its derivative, graphene oxide [73-75]. In the study conducted by Kim and colleagues [69], a Mayer rod was utilized to sequentially deposit P(VB-co-VA-co-VAc) solution in ethanol and 25 mg/ml water-dispersible graphene (WDG) paste onto a cellulose substrate at a speed of 10 cm/s, followed by drying at 60 °C for 1 minute and 10 minutes, respectively. The incorporation of P(VB-co-VA-co-VAc) copolymer as an adhesion layer significantly enhanced the adhesive and mechanical properties of graphene paper due to the potential hydrogen bonding interactions among WDG, P(VB-co-VA-co-VAc) copolymer and cellulose. Compared to the counterpart without P(VB-co-VA-co-VAc) copolymer, graphene paper containing the copolymer exhibited a smoother surface, 23-24 times lower sheet resistance, and improved tensile strength.
In another study, Li et al. coated a graphene/PEDOT: PSS suspension on a 5 cm × 5 cm polyethylene terephthalate (PET) substrate using a Mayer rod with a wire diameter of 6 μm at a speed of 15 mm/s and temperature of 40 °C [70]. The wet film was subsequently placed on an ultrasonic transducer with a vibration power of 1.5 W for 60 s and dried at 40 °C to form a solid film. Introducing substrate vibration during the coating process resulted in improved optical transparency and reduced film thickness of graphene and PEDOT: PSS composite film in comparison with the film prepared without substrate vibration. In addition, there was a threefold

improvement in film conductivity and a nine-times enhancement in carrier concentration after vibration was imposed. Mechanical vibration prevented the agglomeration of graphene and achieved a more uniform distribution of graphene in PEDOT: PSS matrix, thereby improving the charge transfer between graphene and PEDOT: PSS.

Zeng et al. [71] reported the deposition of a 50 μm layer of graphene ink on aluminum foil and printing paper coated with $LiFePO_4$ (LFP) through rod coating, serving as the current collector for a $Li_4Ti_5O_{12}$ (LTO) anode and LFP cathode, respectively. The integrated flexible Li-ion batteries demonstrated good electrochemical performance and excellent structural stability, withstanding 100 bending cycles. Mulberry paper-based sensors were fabricated by rod coating a graphene solution on 16 cm × 20 cm mulberry paper at a speed of 30 mm/s, followed by drying in a vacuum oven at 120 °C for 30 mins [72]. The mulberry paper-based graphene strain sensor exhibited a gauge factor of 3.82, high mechanical resistance of 1.13 MPa, and durability over 1000 bending cycles.

Regarding the deposition of graphene oxide (GO) dispersion on a substrate, the resulting film typically undergoes a reduction reaction to obtain a reduced graphene oxide (rGO) thin film. Wang et al [73]. deposited a suspension of graphene oxide and palladium chloride on a PET substrate using a Mayer rod with a wire diameter of 0.2 mm at a speed of 150 mm/s. GO/Pd film was then reduced by hydrogen at room temperature for 6 hours and immersed in HCl/H_2O_2 solution for 10 minutes to remove palladium. The prepared rGO film was integrated as an electrode for a touch screen, demonstrating superior mechanical flexibility to ITO-based touch screens. In 2014, a flexible alternating current (AC) driven light emitting diode (LED) was developed with rGO function as both the top and back electrode, ZnS: Cu phosphor as the phosphor layer, and GO as a dielectric layer [74]. The rGO and GO films were all fabricated by rod coating. The conductivity of rGO film on a PET substrate was preserved even after bending up to 500 times. The AC-driven

device with a 25 μm GO dielectric layer showed a steady increase of luminance with frequency at 8 V AC bias, and its luminance was twice higher than that of the device with a 35 μm $BaTiO_3$ dielectric layer under a high frequency (1500 Hz). Huang and coworkers [75] rod coated a 1 mg/ml GO solution on polytetrafluoroethylene (PTFE) substrate with a speed of 50 mm/s and dried the wet film in a vacuum box at 50 °C for 24 hours. GO film was peeled off from the PTFE substrate and thermally annealed in an argon atmosphere at 2800 °C with mechanical compaction by graphite planks. The prepared film demonstrated remarkable thermal conductivity, excellent thermal conductivity, and impressive flexibility. There were several beneficial effects of high-temperature annealing treatment, such as healing defects in the structure, reducing the interlayer spacing of rGO sheets and cross-linking adjacent sheets.

The primary objective of this study is to assess the viability of applying the rod coating method to deposit the dispersion of 2D materials other than graphene and its derivatives. Should rod coating prove feasible for the deposition of 2D materials with semiconducting properties in particular, its applicability and benefits could be greatly expanded. In this work, MoS_2 is selected as the representative 2D material because it is a common semiconducting 2D material with a reasonable bandgap and a potentially high in-plane carrier mobility. The properties and applications of MoS_2 are reviewed next.

1.4 Molybdenum Disulfide

1.4.1 Properties of MoS_2

Molybdenum disulfide (MoS_2) belongs to a material class known as transition metal dichalcogenides (TMDs). MoS_2 exists in two distinct phases: a semiconducting 2H phase, where both molybdenum and sulfur atoms are arranged in a hexagonal lattice structure, and a metallic 1T

phase where either the top or lower layer of sulfur atoms in 2H MoS_2 sheet is rotated clockwise by 60°.

The focus of the following discussion is on molybdenum disulfide in the 2H phase. One novel property of MoS_2 is that its band structure depends on the number of S-Mo-S atomic layers. Bulk material and multilayer molybdenum disulfide exhibit an indirect bandgap with a value of 1.2 eV, while monolayer molybdenum disulfide possesses a direct bandgap with a value of approximately 1.8 eV. The conduction band states at the K-point, originating from d orbitals of molybdenum atoms, remain largely unaffected by the number of layers. However, the electronic states near the Γ-point, composed of the d orbital of the molybdenum atom and the P_z orbital of the sulfur atom, are significantly influenced by interlayer coupling [76]. In monolayer MoS_2, both the conduction band minimum (CBM) and valance band maximum (VBM) are located at the K -point. In contrast, in bulk MoS_2, the CBM lies between the K and Γ -points and the VBM is shifted to the Γ-point.

Despite its atomically thin nature, MoS_2 demonstrates relatively strong light-matter interaction, which can be attributed to sharp peaks in the density of states near the band edge. The abundance of available states near the band edge increases the probability of electron-hole pair generation under illumination. The optical absorption of MoS_2 with a few nanometers of thickness is around 10% in the range of visible and near-infrared light [77,78]. There is a gradual increase in both reflectivity and absorption with the thickness of MoS_2, eventually becoming opaque as the number of layers exceeds about 6 to 8 layers [76].

Moreover, high mobility could be reached in MoS_2. At room temperature, the mobility of monolayer MoS_2 ranges from 0.1 to 200 cm^2V/s [79-81]. There is no significant difference in mobility between mechanically exfoliated and chemical vapor deposition (CVD) -grown MoS_2,

indicating the comparable quality of CVD-grown MoS_2 to the mechanically exfoliated one [76]. The mobility of MoS_2 could be further improved by encapsulating MoS_2 with a h-BN layer due to a reduction in carrier scattering [82].

1.4.2 Electronic and Optoelectronic Applications of Solution-Processed MoS_2 Films

1.4.2.1 Thin Film Transistors (TFTs)

A thin film transistor (TFT) is a type of field effect transistor (FET) consisting of a thin film semiconductor channel, a dielectric layer and source, drain and gate electrodes. The fundamental principle governing its operation is the field effect, in which the current flow between the source and drain electrode is modulated by the gate voltage. However, the mobility of TFTs (normally around 0.1–100 $cm^2V^{-1}s^{-1}$ [83]) is lower than FETs in integrated circuits, leading to a reduced switching speed and inferior overall performance. Therefore, TFTs based on amorphous and polycrystalline silicon are commonly used in flat panel displays and touchscreens. Even though TFTs based on amorphous silicon have reached a level of sophistication, there still are some objectives to pursue in the research field. One such goal is simplifying the fabrication process to reduce production costs. Another target is to fabricate flexible TFTs. In the quest for next-generation TFTs, solution-processed molybdenum disulfide emerges as a promising candidate due to its novel electrical properties and flexibility.

Xi et al. [84] developed an area-selective solution deposition method to deposit MoS_2 film by submerging a SiO_2/Si substrate with Cr/Au electrodes in a mixture of precursor a solution $(NH)_4MoS_4$ and the reducing agent hydrazine hydrate at 90 °C for 27 minutes, followed by thermal annealing in N_2 at 350 °C for an hour to remove unreacted precursors. With the gold surface as a catalyst, MoS_2 film was selectively deposited as the channel of TFTs with a thickness of 11 nm. The TFTs exhibited a field-effect mobility of 0.4 $cm^2 V^{-1}s^{-1}$ and an on/off ratio of 10^6.

In a study by Zeng and colleagues [67], a MoS_2 dispersion with a concentration of 0.206 mg/ml was prepared by a two-step liquid phase exfoliation process and deposited onto the substrate with pre-patterned interdigital electrodes through spray coating. The carrier mobility of the fabricated TFTs with 200 nm thick MoS_2 channel was around 10^{-4} cm^2 $V^{-1}s^{-1}$, a relatively low value. The poor performance of TFTs based on solution-processed MoS_2 could be attributed to the quality of the material, as flakes obtained from liquid phase exfoliation are prone to defects, small lateral size, and a broad distribution of flake thickness. To address these issues, it is imperative to develop a solution processing method that produces high-quality materials and select a suitable deposition method to achieve a high-quality uniform thin film in an economical and scalable manner.

An electrochemical intercalation method with quaternary ammonium bromide was reported to produce high-quality MoS_2 nanosheets with a narrow thickness distribution and electron mobility of about 10 cm^2 $V^{-1}s^{-1}$, which is ten times greater than the mobility of Li-exfoliated MoS_2 nanosheets [56]. Regarding the fabrication of TFTs, an ink solution of exfoliated MoS_2 in ethanol was spin-coated three times on a 4-inch wafer of SiO_2/Si substrate, and the thickness of the resulting film was approximately 10 nm. The TFTs exhibited field-effect mobility ranging from 7 to 11 cm^2 $V^{-1}s^{-1}$ and an on/off ratio of 10^6.

Gomes and coworkers [85] deposited a MoS_2 thin film with a thickness of 2.07 nm on a sapphire substrate through spin coating molybdenum(V)-chloride precursor solution in 1-methoxy-2-propanol on the substrate, followed by pre-annealing in N_2 at 150 °C for 10 minutes, annealing in a mixture of hydrogen and argon gas with pure sulfur at 900 °C for an hour, and post-annealing in Ar at 980 °C for another hour. The top-gate top-contact ionic liquid-gated TFTs possessed a high field-effect mobility of 12.07 cm^2 $V^{-1}s^{-1}$ and an on/off ratio of 10^6.

A layer-by-layer assembly method of a MoS_2 dispersion prepared by electrochemical intercalation involved sequential immersion of pre-cleaned substrates (SiO_2/Si, PI or PET) in poly dimethyl diallyl ammonium chloride (PDDA) and MoS_2 dispersion, followed by rinsing with DI water and drying after each adsorption, for one complete cycle. [86] Repeating the cycles could achieve multiple layers of PDDA and MoS2 on a substrate. To fabricate a TFT with ionic liquid gel as the top gate, layer-by-layer assembly of MoS_2 film was performed on SiO_2/Si substrate patterned with photoresist and conducted a subsequent lift-off process with acetone. Two bilayers of PDDA/MoS_2 with a thickness of 12.8 nm were immersed in 10 mg/ml bis (trifluoromethane) sulfonimide (TFSI) in 1,2-dichloroethane at 80 °C for two hours and then thermally annealed at 300 °C in argon for another two hours to reduce doping. The field-effect mobility and on/off ratio were 9.8 $cm^2 V^{-1}s^{-1}$ and 2.1×10^5, respectively.

In a similar process to the work of Gomes et al., a 0.0125M water-based $(NH_4)_6Mo_7O_{24}\cdot4H_2O$ precursor solution was spin-coated on a SiO_2/Si substrate and the film was annealed at 1000 °C for an hour to obtain a thin film with a thickness of 2.6 nm [87]. The film was then transferred to an Al_2O_3/Si substrate using polymethyl methacrylate (PMMA) in order to fabricate TFTs with a field-effect mobility of 8.5 $cm^2 V^{-1}s^{-1}$ and an on/off ratio of 10^5. For an overview of the reported performance of the solution-processed MoS_2-based TFTs, please refer to Table 1.2. According to the summarized results, further improvements in the electrical performance of solution-processed MoS_2-based TFTs are still required for their practical applications as the field-effect mobility values reported in the literature are relatively low. The two essential objectives in the field involve the optimization of solution-based exfoliation methods and investigation into new thin film deposition methods [29]. TFTs based on solution-processed 2D

materials are adequate for applications in low-resolution displays which do not demand high carrier mobility, such as liquid crystal displays (LCDs).

Table 1-2 Summary of the electrical performance of TFTs based on solution-process MoS_2 in the literature.

Deposition method	TFT Structure	On/Off ratio	Field-effect Mobility ($cm^2 V^{-1}s^{-1}$)	Reference
Selective Area Solution Deposition	MoS_2(11nm)/Au(100nm)/ Cr(10nm)/SiO_2(350nm)/P^{++} Si	10^6	0.4	[84]
Spray Coating	MoS_2(200nm) /Au(30nm)/ITO (10nm)/SiO_2(230nm)/n^{++} Si		10^{-4}	[67]
Spin Coating	Au(50nm)/Ti(30nm)/MoS_2(10nm)/ SiO_2(90nm)/ Si	10^6	7-11	[56]
Wet Chemical Synthesis	Au(1mm)/Ionic liquid gel(4um) /Au(40nm)/MoS_2(2.07nm)/sapphire	10^6	12.07	[85]
Layer-by-Layer Assembly	Au(45nm)/Cr(5nm)/Ionic liquid/Au(45nm)/Cr(5nm) /PDDA/MoS_2/ SiO_2/Si	2.1×10^5	9.8	[86]
Wet Chemical Synthesis	Al(100nm)/MoS_2(2.6nm)/ Al_2O_3(80nm) /Si	$(0.8 \pm 0.3)\times10^5$	7.9 ± 0.6	[87]

1.4.2.2 Photodetectors

A photodetector is a device that converts light into an electrical signal, including photocurrent or photovoltage, through several different photocurrent generation mechanisms. The photoconductive effect, for instance, involves the separation of electron-hole pairs generated by the incident photons under an applied electric field, leading to an increase in total current. The photogating effect could be viewed as a special case of the photoconductive effect. Localized states near the band edge of the semiconductor, arising from defects in the semiconductor lattice or adsorbates on the interface between the semiconductor and substrate, trap one type of carrier generated by light illumination to function as local gates and thus modulate the conductance of the

semiconductor. In practice, there is not a clear distinction between the photoconductive and photogating effect because both effects can take place in the same device. The photovoltaic effect, which involves the separation of photo-generated electron-hole pairs by an internal electric field, is a common photocurrent generation mechanism in photodetectors based on heterojunctions. The photo-thermoelectric effect refers to a phenomenon where non-uniform heating of the semiconductor induced by localized light illumination generates a potential difference across the semiconductor and in turn facilitates a current flow. In contrast, the photo-bolometric effect is associated with a homogeneous temperature profile in a semiconductor induced by uniform light illumination leading to a change in the conductance of the semiconductor. A device based on the photo-bolometric effect requires applied bias voltage to produce current flow in the semiconductor.

The performance of a photodetector is evaluated by a set of parameters, known as the figures of merit. Responsivity (R) is defined as the ratio of photocurrent (I_{ph}) to the incident optical power (P), $R = \frac{I_{ph}}{P}$. Detectivity (D*) is an indicator of a photodetector's ability to detect the weakest optical signal. The response speed of a photodetector is characterized by response time. The time required to change from 10% to 90% of the generated signal is referred as rise time (T_{rise}), and from 90% to 10% is denoted as the fall time (T_{rise}). Generally speaking, high values of responsivity and detectivity are desirable for a photodetector, while its response time should be minimized.

The application of 2D materials in optoelectronics constitutes an active research area, which can be attributed to their pronounced light-matter interactions and possible non-linear optical characteristics. Mechanically exfoliated or CVD-grown 2D materials are commonly employed in the fabrication of photodetectors, primarily due to the exceptional quality of the material. However, limited efforts have been devoted to the advancement of photodetectors based

on solution-processed 2D materials as it is challenging to achieve consistent and reliable material quality through solution-processing steps. Variations in the crystalline structure and properties of the resulting film could stem from factors like solvent selection, deposition conditions and post-deposition treatments, thereby directly influencing the performance and reproducibility of photodetectors. Nonetheless, solution-processing methods present substantial potential for cost-effective and scalable productions of large-area flexible optoelectronic devices in next-generation imaging, sensing and communication systems.

Cunningham et al. [88] prepared a dispersion of MoS_2 nano-platelets via liquid phase exfoliation and fabricated a vertical photodetector based on a MoS_2 film formed by the Langmuir-Blodgett method with a thickness of 6 μm. The responsivity of the photodetector at low intensity was approximately 0.1 mA/W with a bias voltage of 15 V. In another study, an ink of MoS_2 with an estimated concentration of 0.1 mg/ml was directly deposited on SiO_2/Si substrate in uniform, high-quality patterns through inkjet printing [89]. The printed photodetector with a structure of TFT exhibited a fast photoresponse at V_g = 0 V and V_d = 1 V, in which the device current speedily increased or decreased and subsequently returned to the dark current value as the light was switched on and off periodically at an interval of 5 s. The responsivity of the photodetector was estimated to be 36 ± 7 μA/W. Lim and colleagues [90] deposited a film of MoS_2 via spin coating $(NH_4)_2MoS_4$ precursor solution onto the substrate, followed by annealing at 280 °C in N_2 for 30 minutes and subsequent annealing at 450 °C under 100 sccm flow of H_2 with N_2 for another 30 minutes. An array of MoS_2-based photodetectors fabricated on a 4-inch SiO_2/Si wafer yielded a uniform photocurrent distribution regardless of device location. The photocurrent of the photodetectors was linearly dependent on the bias voltage and illumination power. Flexible MoS_2-

based photodetectors fabricated on polyimide (PI) substrate demonstrated excellent bendability, revealing only a 5.6% decrease in photocurrent after 10^5 cycles of bending.

Seo and coworkers [91] performed subsequent inkjet printing of MoS_2/Ethyl cellulose (EC) ink and graphene/EC ink on the substrate (glass or polyimide film) at 25 °C and 30 °C, respectively. The fully printed MoS_2 photodetector on glass that was thermally annealed at 400 °C for three hours under H_2/Ar demonstrated a responsivity of 1 mA/W at an incident wavelength (λ) of 515.6 nm with a relatively weak dependence on illumination power, a rapid photoresponse of less than 150 μs and a detectivity of 4.31×10^7 Jones. The flexible MoS_2 photodetector on a polyimide substrate with photonic annealing treatment possessed a high responsivity exceeding 50 mA/W at an irradiation intensity of 0.6 W/cm^2, an enhanced detectivity of 3.18×10^9 Jones and maintained its sensitivity (ratio of photocurrent over dark current) over 500 bending cycles. Through vacuum filtration, Park et al. [58] prepared a film of MoS_2 on an alumina membrane disk using a dispersion of MoS_2 functionalized with dodecanethiol (DDT) and transferred the film onto SiO_2/Si substrate with silicon gel film. After stacking several layers of MoS_2 film on the target substrate, it was immersed in MeOH for 30 minutes. A photodetector based on 5 stacked layers of MoS_2 film (~ 6 monolayers of MoS_2) showed a responsivity of 2 mA/W and a responsivity of 10^8 Jones at $V_d = 1$ V and $V_g = 0$ V under the illumination of a white LED. With a negative gate voltage of -2 V, the responsivity experienced an eight-fold increase to 36 mA/W at $V_d = 2$ V compared with the value without gating (4 mA/W). In 2022, a paper reported the fabrication of a MoS_2-based photodetector on cellulose paper through screen printing of interdigital electrodes with conductive carbon ink and spray coating a MoS_2 dispersion [68]. The device was calendered between rollers to reduce the inter-nanosheet junction resistance. The responsivity of the photodetector was 6 mA/W

under white illumination with a power density of 2.5 W/cm^2 and the photocurrent underwent a 27% decrease in its value under bending with respect to the flat condition.

The performance of photodetectors based on solution-processed MoS_2 in the literature is summarized in Table 1.3. There is still room for improvement in the responsivity and detectivity of photodetectors. Engineering the band structure of MoS_2 via selective doping or introducing defects in the lattice structure could either facilitate the separation of photogenerated carriers or reduce the band gap. Integration with other solution-processed 2D materials emerges as a promising avenue to broaden the spectral response of photodetectors based on solution-processed MoS_2 and achieve a high responsivity without compromising the response speed. Another area of concern is the stability and long-term durability of solution-processed MoS_2-based photodetectors at ambient conditions. Moisture and other environmental factors could degrade the properties of the material over time, consequently leading to deterioration in device performance. Encapsulation and protective coatings potentially play a vital role in prolonging the operational lifespan of the device.

Table 1-3 Summary of the performance of photodetectors based on solution-process MoS_2 in the literature.

Deposition method	Device Structure	Performance Parameter	Reference
Langmuir-Blodgett Method	Au(50nm)/MoS_2(6μm)/ITO	R ~ 0.1 mA/W at V_d =15 V	[88]
Inkjet Printing	Ag/MoS_2/SiO_2(300nm)/Si	T_{rise} = 60 ms, T_{fall} = 570 ms, R = 0.036 mA/W at V_d =1 V, V_g = 0 V	[89]
Wet Chemical Synthesis	Au(100nm)/MoS_2/polyimide	T_{rise} = 13 s, T_{fall} = 30 s at V_d = 20V	[90]
Inkjet Printing	Graphene/MoS_2/glass	R = 1 mA/W, D* = 4.31×10^7 Jones λ = 515.6 nm at V_d = 40 V T < 150 μs at V_d = 10 V	[91]
	Graphene/MoS_2/polyimide	R > 50 mA/W at V_d = 40 V,0.6 W/cm^2 D* = 3.18×10^9 Jones	
Vacuum Filtration	Au(40nm)/Cr(5nm)/MoS_2/SiO_2(300nm)/Si	R = 2 mA/W, D* = 1×10^8 Jones T_{rise} = 7 s, T_{fall} = 8 s at V_d =1 V, V_g = 0 V	[58]

		R = 36 mA/W at V_d = 2 V, V_g = -2 V	
Spray Coating	Carbon Electrodes/MoS_2 (30-40μm)/Cellulose	R = 6 mA/W at V_d = 20 V, 2.5 W/cm^2	[68]

1.4.2.3 Printed Electronics

Printed electronics refer to electronic devices and circuits fabricated using various printing processes, such as inkjet printing, screen printing, gravure printing, and flexography. In contrast to conventional electronics fabrication, which relies on subtractive methods like etching and lithography, the fabrication of printed electronics employs additive techniques in ambient conditions to directly deposit patterns of electronic components onto a variety of substrates, including paper, fabrics, and plastics like polyethylene terephthalate (PET). The indispensable component of printed electronics is printable formulation or ink. The inverse Ohnesorge number (Z) is an important parameter to predict the ability of a certain type of ink to form stable drops, defined as $z = \frac{\sqrt{\gamma\rho\alpha}}{\eta}$, where γ represents surface tension, ρ is density, α denotes the set nozzle diameter and η is viscosity [29]. The formation of stable drops is reported to occur as Z falls between 1 and 14 [29]. Accordingly, two essential principles of ink design involve reducing surface tension and increasing viscosity [29]. The use of solution-processed 2D materials as printable formulation appears to be an ideal choice for developing large-area flexible printed electronics because of their diverse electrical and optical properties.

McManus and colleagues [65] have presented a general method to produce water-based, inkjet-printable, and biocompatible formulations of two-dimensional materials. Two modifier agents were introduced to enhance the printing ability of the dispersion in water, including a non-ionic surfactant triton X-100 to reduce surface tension and a co-solvent propylene glycol to improve viscosity and biocompatibility. In addition, a non-toxic and environmental-friendly binder

Xanthan Gum was added after exfoliation to curtail re-dispersion at the interface of multiple stacked layers. The versatility of this method was demonstrated in the preparation of water-based, biocompatible, and stable inks of graphene, WS_2, MoS_2 and h-BN with a Z value ranging from 20 to 22. Although Z is larger than 14, stable droplets could still form. An array of photodetectors with graphene as top and bottom electrodes and MoS_2 as a photosensitizing layer were inkjet-printed on a glass substrate. The investigation into the biocompatibility of ink revealed no significant adverse response, thus paving the way for potential applications of 2D material ink formulations in smart packaging and identification tags for food, beverages, pharmaceuticals, and consumer products.

In a separate study, Mondal et al. [92] developed an ink of MoS_2 through liquid phase exfoliation, employing ethylenediamine (EDA) for adsorption. During the fabrication of inkjet-printed TFTs, formulated MoS_2 ink was printed on top of patterned electrodes (either Sn-doped indium oxide (ITO) or Cr/Au) functioning as the channel, with a subsequent printing of silver nanoparticle ink to reduce the effective channel length. The device underwent curing on a hot plate at 200 °C in air and thermal annealing at 300 °C in argon. A printable composite solid polymer electrolyte (CSPE) and a poly(3,4-ethylenedioxythiophene) polystyrene sulfonate (PEDOT: PSS) were printed as the gate insulator and gate electrode to conclude the fabrication. TFTs with ITO passive electrodes demonstrated an average on/off ratio of $(4 \pm 1) \times 10^5$, while devices with gold passive electrodes exhibited an improved average on/off ratio of $(3 \pm 1) \times 10^6$.

A persistent challenge encountered in solution-processed 2D material inks is the formation of controlled and stable patterns [29]. The value of Z reported in the literature [65] is still larger than 14, limiting its further applications, particularly in extended printing sessions [29]. One approach to address this issue is utilizing polymer binders in ink formulations [93]. This method involves

isolating exfoliated 2D materials from their initial suspensions and re-dispersing them in solvents with designated polymer binders. This approach does not only reduce the value of Z but also facilitates the preparation of highly concentrated inks [93]. Evidently, the significant obstacle lies in developing scalable inks that would enable efficient and uniform large-scale printing of electronics based on 2D materials with high quality. One viable strategy to produce high-performance devices is integrating 2D materials with other functional materials, including conducting or semiconducting polymers, carbon nanotubes, quantum dots and biocompatible materials.

1.5 Thesis Organization

The motivation for this thesis is to investigate the feasibility of rod coating as a method for the deposition of solution-processed MoS_2 film, which stems from the recognized limitations of commonly employed film assembly methods in the literature regarding scalability, cost-effectiveness, and simplicity. Given the versatility of rod coating as a thin film deposition method, the successful fabrication of MoS_2 film would indicate the possibility of extending this method to the deposition of various 2D materials. In Chapter 2, rod coating is applied to deposit a thin film of MoS_2 flakes. This chapter delves into the systematic investigation of five experimental parameters to optimize the surface coverage of MoS_2 flakes and minimize the sheet resistance of the prepared film. Subsequent to the preparation of the optimal MoS_2 film, film morphology is characterized by a scanning electron microscope and film resistivity is assessed through the measurement of sheet resistance using a four-point probe. In Chapter 3, the optimized MoS_2 thin film is integrated into thin film transistors as a semiconductor channel. A comprehensive overview of the fabrication process is presented. Two-terminal and three-terminal electrical

characterizations of the thin film transistor provide qualitative information about the electrical connection between flakes within the thin film. Chapter 4 presents another application of rod coating to deposit silver nanowires. The silver nanowire network is integrated as a transparent electrode in a WS_2-based light emitting device (LED), demonstrating a reasonable luminance and bidirectional emission as a transparent LED. Further enhancement in the performance of the silver nanowire electrode is still needed in the future. Finally, Chapter 5 serves as the concluding segment of the thesis, summarizing the key findings and contributions. It also provides an outline for the work in the future.

Chapter 2 Rod Coating MoS_2 Flake Films

2.1 Introduction

As elucidated in Chapter 1, rod coating is suitable for roll-to-roll production in the industry. This method facilitates the direct deposition of solution-processed two-dimensional (2D) materials onto diverse substrates over a large area while allowing for the control of film thickness through a simple and fast operation procedure. In contrast to other solution-based deposition techniques, rod coating distinguishes itself as a promising approach for the thin film deposition of 2D materials, which is attributed to its simplicity, cost-effectiveness, versatility, and scalability. Despite these merits, the potential of rod coating remains underexplored, primarily finding application in the deposition of graphene and graphene oxide.

In this chapter, rod coating is employed to deposit a dispersion of molybdenum disulfide (MoS_2) flakes on SiO_2/Si substrates, demonstrating the viability of rod coating as a method for the assembly of 2D materials. Molybdenum disulfide was selected because of its semiconducting nature characterized by a layer-dependent bandgap and potentially high in-plane carrier mobility. These attributes make it ideal for deployments as a semiconductor channel in thin film transistors and a light-sensitizing element in photodetectors. The goal is to use the rod coating process to achieve a thin film of MoS_2 with continuous coverage of MoS_2 flakes and a minimized sheet resistance for its integration into thin film transistors later. Several experimental parameters were systematically investigated to optimize the film quality as well as electrical properties. Once an optimized film was obtained, characterization was conducted to assess film morphology and sheet resistance.

2.2 Experimental Procedure

2.2.1 Concentrating Dispersion

Monolayer MoS_2 flakes dispersed in ethanol at concentrations of 1 mg/ml and 5 mg/ml were purchased from ACS materials (Pasadena, USA). According to the information provided by the vendor, the average diameter of the flakes ranges from 0.2 to 5 μm, with the majority falling between 1 and 3 μm. The thickness of the flakes is approximately 1 nm. Initially, these two solutions were deposited on the substrates via rod coating. Subsequently, to enhance the surface coverage of MoS_2 flakes, the MoS_2 solution with a concentration of 5 mg/ml was concentrated into higher concentrations, for instance, 50 mg/ml and 100 mg/ml. Concentrating MoS_2 dispersion was conducted by a Scilogex mini centrifuge with a fixed rotating speed of 7000 rpm. To achieve this, the MoS_2 solution was transferred from its original container into 1.5 ml centrifuge tubes by a pipette and centrifuged for 24 hours. The volume of solvent to be removed was calculated based on the target concentration. For a target concentration of 50 mg/ml, which is ten times as the concentration of the starting solution, the total volume of the solution needs to be 0.15 ml, indicating 1.35 ml of the solution after centrifugation ought to be extracted. This calculation process was also applied for a target concentration of 100 mg/ml. A portion of the supernatants was pipetted out and centrifuged the solution for another 24 hours. Again, supernatants were extracted using a pipette to reach the desired volume as calculated previously. After the target concentration was reached, the solution was placed under an ultrasonication probe for one minute to improve the dispersion of MoS_2 flakes. It should be noted that the target concentration is an upper limit of the actual concentration; the actual or real concentration would be lower than the target value because of the incomplete separation of solvent during the centrifugation process.

2.2.2 Substrate Treatment

A 4-inch wafer of heavily p-doped silicon with a layer of 300 nm silicon dioxide on top (University wafer, resistivity ranging from 0.001 to 0.005 Ω·cm) was first treated with oxygen plasma in a plasma strip/descum system (CV200RFS, Yield Engineering Systems) at an RF power of 500 W, pressure of 800 mTorr, temperature of 25 °C and oxygen flow rate of 50 standard cubic centimeters per minute (sccm) for one minute. After, a layer of positive photoresist, Shipley 1811 (Microposit), was spin-coated onto the wafer with a spin speed of 3000 rpm, followed by a soft bake at 115 °C for one minute. The purpose of this photoresist layer was to shield the substrate from debris and particles in the following dicing step. The wafer was then cut into 2 cm × 2 cm pieces by a dicing saw (DAD3240, Disco Corporation).

The standard cleaning procedure of 2 cm × 2 cm Si/SiO_2 substrates involved immersing the substrates in acetone, IPA, and DI water in an ultrasonication bath for 280 seconds each. Afterwards, the substrates were blown dry by N_2. It was found to be necessary to further enhance the wetting of the MoS_2 dispersion and its adhesion to the substrate through surface treatment. Two surface treatments were considered. The first one just replaced DI water in the standard cleaning process with ethanol which is the solvent of the MoS_2 solution. The second one was treating the substrate with a piranha solution (H_2SO_4: H_2O_2 = 4:1) for 15 minutes following the standard cleaning process. Subsequently, the substrate surface was activated by oxygen plasma for 10 minutes (Recipe: RF power: 500 W; Pressure: 800 mTorr; Temperature: 25 °C; O_2 flow rate: 50 sccm) prior to the coating of MoS_2 flakes. The effects of these two surface treatments were evaluated by measuring the contact angle of DI water on substrates with a contact angle goniometer (190 CA, Rame-Hart Instrument Co.) immediately after the surface treatments (Figure 2.1). A droplet of DI water was dispensed onto a substrate placed on the adjustable sample stage below,

and an image of the droplet on the substrate was subsequently captured by a camera positioned opposite to the light source for analysis by the software.

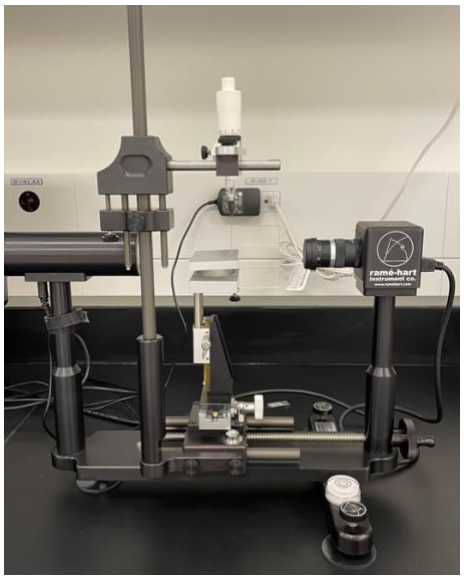

Figure 2.1 Setup of the contact angle measurement.

2.2.3 Rod coating

13 μL of MoS_2 solution was first drop cast evenly on one side of the substrate. A Mayer rod (RDS Specialties) was gently rolled down the substrate with constant pressure and speed. This step was repeated for the MoS_2 solution pipetted along the other three edges of the substrate. The thickness of the rod-coated film is determined by the distance between the grooves on the Mayer bar. A Mayer rod with a larger wire diameter (rod number) yields a thicker film. Furthermore, by increasing the number of coats from four to eight or sixteen, higher surface coverage of MoS_2 flakes can be achieved.

2.2.4 Thermal Annealing

After the rod coating of MoS_2 film on Si/SiO_2 substrates, the as-prepared film was subjected to thermal annealing to improve the contacts between individual flakes, thereby

enhancing the conductivity of the film. In order to determine the annealing temperature that optimizes the film's electrical properties, MoS_2 film deposited on two 2 × 2 cm Si/SiO_2 substrates (number of coats: 16; MoS_2 dispersion concentration: 100 mg/ml; surface treatment of Si/SiO_2 substrates: piranha and oxygen plasma treatment) were cut into eight approximately 1cm × 1 cm small pieces using a diamond scribe. These small pieces were subsequently annealed at several different temperatures, 150 °C, 200 °C, 300 °C, 350 °C, and 400 °C. For annealing temperatures equal to or below 200 °C, the thermal annealing process was carried out in a vacuum oven for 30 minutes. Annealing at temperatures equal to or above 300 °C was achieved in a rapid thermal processor (AccuThermo AW 610, Allwin21Corp) in an argon environment for 30 minutes. Even though there were variations among samples regarding the coverage of MoS_2 flakes and film uniformity, the sheet resistance of these small pieces provided insight into the optimal thermal annealing temperature.

2.2.5 Film Characterization Methods

The characterization of prepared MoS_2 film involves inspecting film morphology and surface coverage of MoS_2 flakes through scanning electron microscopy (SEM), measuring sheet resistance with a four-point probe, and determining film thickness using either a profilometer or atomic force microscopy (AFM).

MoS_2 films were rod-coated on 2 cm × 2 cm silicon substrates (University Wafer, resistivity ranging from 1 to 10 Ω·cm) without SiO_2 for SEM imaging. SEM images of MoS_2 films were taken by a Hitachi SU5000 Field Emission Scanning Electron Microscope using the secondary electron detector.

Two different four-point probe setups were employed to measure the sheet resistance of MoS_2 film on 2 cm × 2 cm Si/SiO_2 substrates. The first one was an Ossila four-point probe whose sheet resistance measurement range is between 100 mΩ/□ and 10 MΩ/□. The target current of the outer two probes was set to 10 μA and the voltage difference between the inner two probes was measured 25 times to provide a time-averaged result. The probes were placed at 6 different positions on the MoS_2 films, and the measured values were averaged to provide an overall sheet resistance of the prepared film. If sheet resistance could not be measured by Ossila four-point probe, sheet resistance measurements were performed with a four-point robe connected to a Keithley 2400 Source Meter system in 4-wire resistance sense mode. The sheet resistance values were obtained by multiplying the instantaneous resistance value read from the digital multimeter with the Van der Pauw constant, which is approximately equal to 4.532. As in the previous case, the sheet resistance values were measured at 6 different locations on a MoS_2 film and averaged. However, the sheet resistance values obtained from the second measurement setup only provide an area-averaged result rather than a time and area-averaged result like that from the first setup.

A step-like structure was produced for film thickness measurement by removing film near the edge of the substrate with a Q-tip in acetone. A profilometer (DektakXT, Bruker) was used to obtain a large scan size (~ 80 μm) across the boundary for films with thicknesses larger than 100 nm. AFM (Dimension FastScan, Bruker) was used for measuring films with thicknesses below 100 nm. Some inaccuracies in the film thickness measurement originated from inadvertent thinning of the film on the boundary when removing the film near the edge.

2.3 Effect of Rod Coating Parameters

A solution-processed MoS_2 film, to be integrated into electronic and optoelectronic devices, requires a continuous coverage of MoS2 flake, a relatively low surface roughness, a controllable film thickness and satisfying electrical properties. To determine how to obtain a MoS_2 film with optimal film morphology and desirable electrical properties through rod coating, five different parameters were investigated: the wire diameter of the Mayer rod (rod number), the concentration of flakes in the dispersion, the number of coats, hydrophilicity/hydrophobicity of the substrate (contact angle) and thermal annealing temperature. The systematic optimization process for each parameter was sequentially conducted following the aforementioned order, while other parameters remained the same.

2.3.1 Rod number

The influence of rod number (wire diameter) on the surface coverage of MoS_2 flakes was investigated, which involved the deposition of 1 mg/ml MoS_2 solution on 2 cm × 2 cm Si substrates for 4 coats, employing Mayer rods with different rod numbers. At first, a rod with a wire diameter of 0.25 mm (RDS #10) was selected to deposit MoS_2 flakes. The SEM images in Figure 2.2 demonstrate an extremely low surface coverage of MoS_2 flakes. Numerous individual flakes are distributed across the surface without connecting to form continuous coverage. Subsequently, a rod with a larger wire diameter was used to coat MoS_2 flakes. Two samples with 4 coats of MoS_2 dispersion on the substrate were prepared using a Mayer rod of number 60 (wire diameter: 1.52 mm) and 95 (wire diameter: 2.41 mm), respectively. SEM characterization (Figure 2.3, 2.4) confirms that the surface coverage is improved with the use of a rod with a larger rod number. Despite the improvement in surface density, the overall coverage of MoS_2 flakes on the substrate

remains insufficient to form a continuous flake film. When rods with a higher rod number were utilized, there were remaining droplets of solution on the edge opposite to the one where MoS_2 dispersion was pipetted after rolling the rod across the substrate, resulting in greater surface coverage near the edge compared to the central region. As 2.41 mm is the largest wire diameter of a Mayer rod that could be provided by the manufacturer, further enhancement of surface coverage would require an increase in the concentration of MoS_2 dispersion.

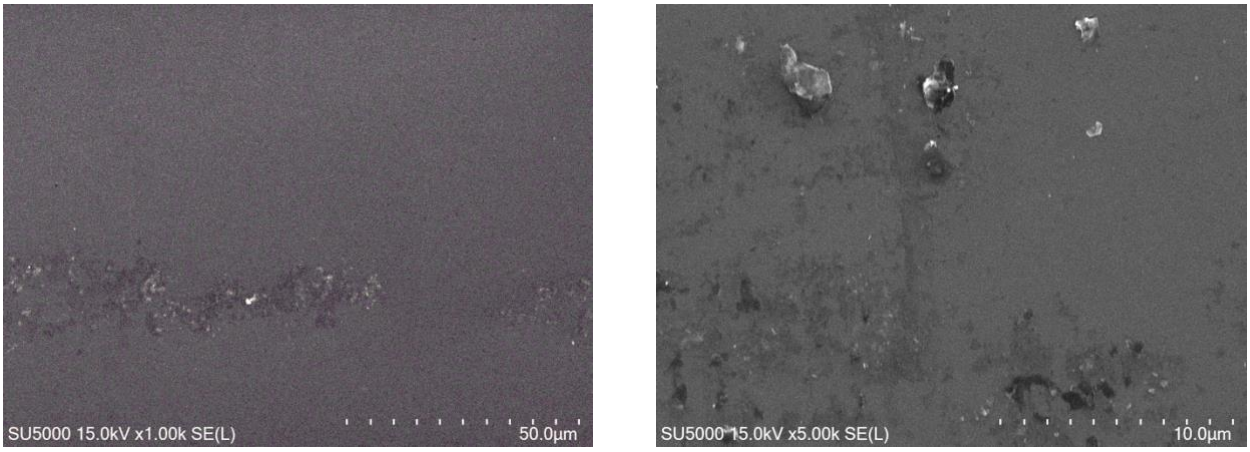

(a) (b)

Figure 2.2 a) and b) SEM images of rod-coated 1 mg/ml MoS_2 solution on 2 cm × 2 cm Si substrate using rod RDS #10 for 4 coats.

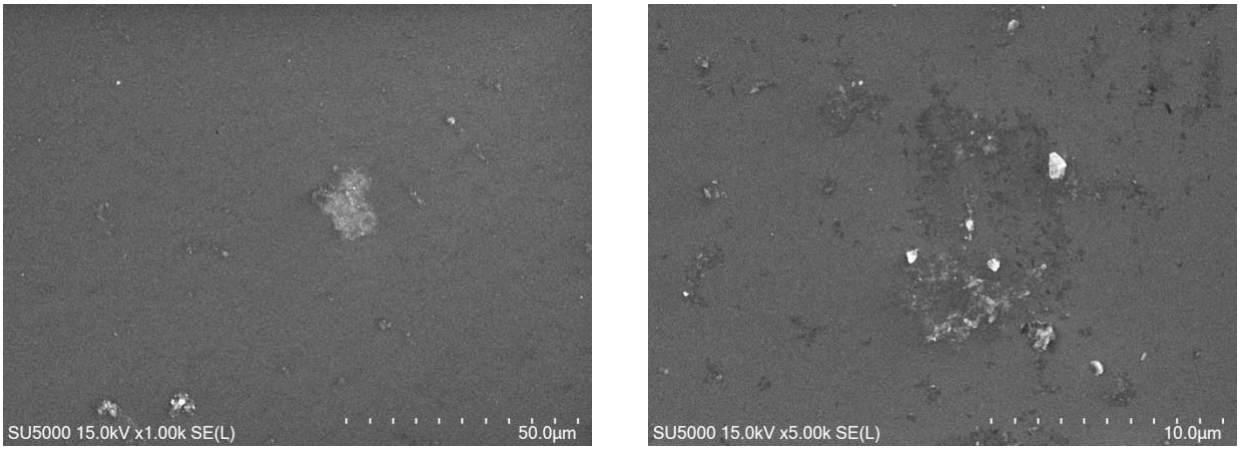

(a) (b)

Figure 2.3 a) and b) SEM images of rod-coated 1 mg/ml MoS_2 solution on 2 cm × 2 cm Si substrate using rod RDS #60 with 4 coats.

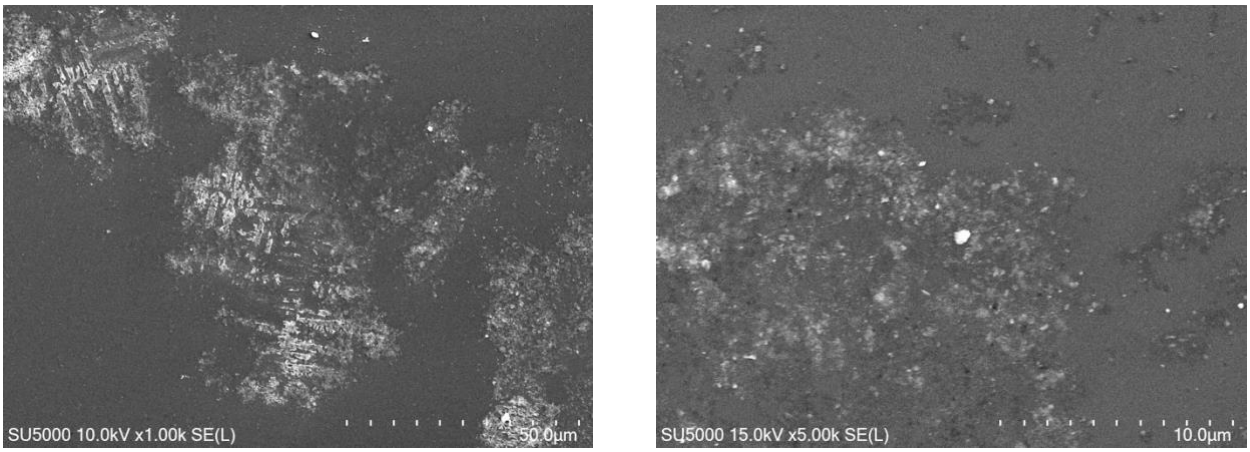

(a) (b)

Figure 2.4 a) and b) SEM images of rod-coated 1 mg/ml MoS_2 solution on 2 cm × 2 cm Si substrate using rod RDS #95 with 4 coats.

2.3.2 Solution concentration

In this subsection, MoS_2 dispersions at various concentrations were coated on 2 cm × 2 cm Si substrates with 4 coats by a rod of number 95. The initial concentration employed was 5 mg/ml. There was a noticeable improvement in surface coverage when compared to the counterpart prepared by 1mg/ml MoS_2 solution, as shown in Figure 2.5. It was observed that certain regions of the substrate exhibited higher surface coverage, while the surface coverage on other parts was still relatively low. With the aid of a centrifuge, the concentration of MoS_2 solution was increased to 50 and 100 mg/ml, corresponding to a 10 and 20-fold increase in comparison with the initial concentration of 5 mg/ml, respectively. SEM characterization (Figure 2.6 and 2.7) indicate that the area of the substrate covered by MoS_2 flakes rose as a dispersion with a higher concentration was utilized. However, the problem of residual droplets mentioned in the previous subsection became more pronounced when using MoS_2 solution at a higher concentration, again resulting in greater

surface coverage near the edge compared to the central region. Although a significant enhancement in surface coverage was achieved with 100 mg/ml MoS_2 dispersion, there were still a relatively small number of areas on the substrate that were not covered by MoS_2 flakes. To obtain a continuous flake film, it would be necessary to increase the number of coats.

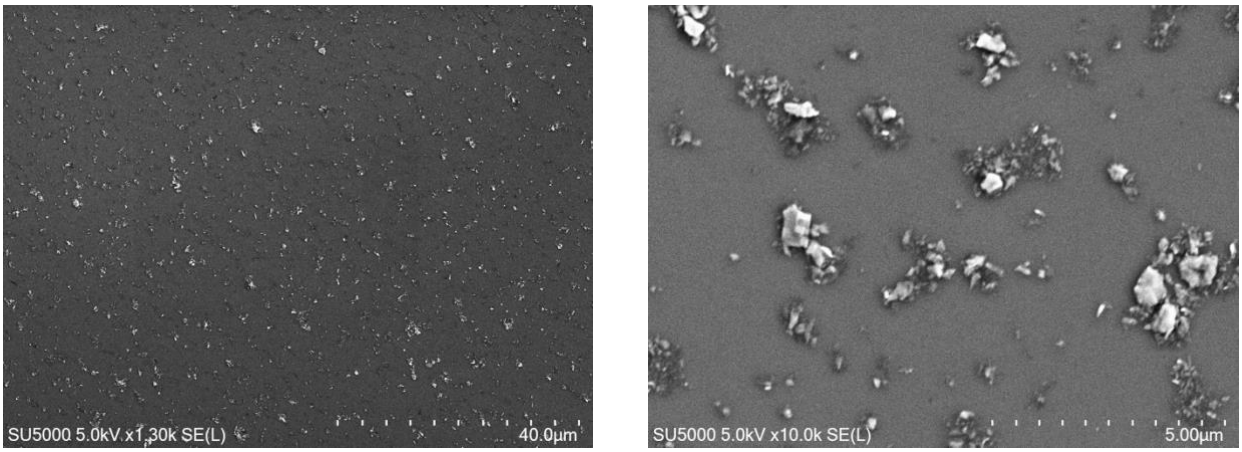

(a) (b)

Figure 2.5 a) and b) SEM images of rod-coated 5 mg/ml MoS_2 solution on 2 cm × 2 cm Si substrate using rod RDS #95 with 4 coats.

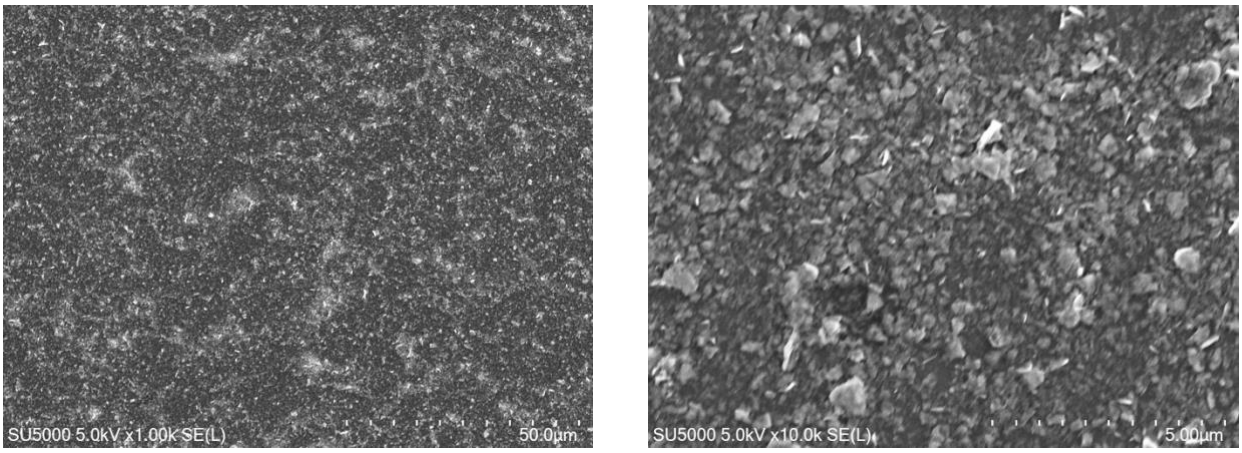

(a) (b)

Figure 2.6 a) and b) SEM images of rod-coated 50 mg/ml MoS_2 solution on 2 cm × 2 cm Si substrate using rod RDS #95 with 4 coats.

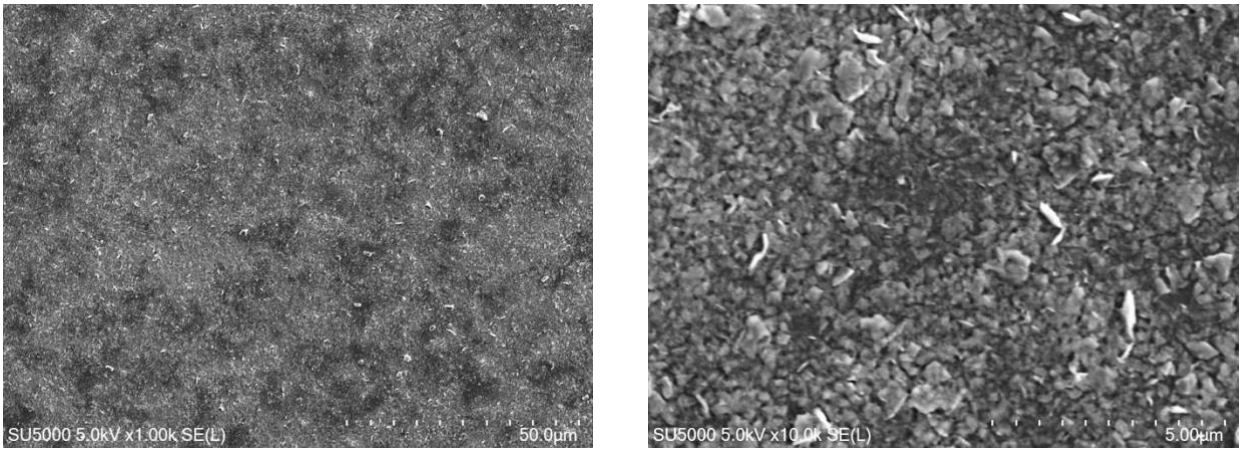

(a) (b)

Figure 2.7 a) and b) SEM images of rod-coated 100 mg/ml MoS_2 solution on 2 cm × 2 cm Si substrate using rod RDS #95 with 4 coats.

2.3.3 Number of coats

A 100 mg/ml MoS_2 solution was coated on silicon substrates with a rod of number 95 for 8 and 16 coats to determine the optimal number of coats. Nearly complete coverage of MoS_2 flakes on the substrates was achieved by 8 coats based on SEM imaging (Figure 2.8). On the other hand, 16 coats improved the uniformity of the film in the central region and increased the likelihood of flakes overlapping. Consequently, a flake film with a larger number of coats is expected to possess an increased thickness and provide more conductive pathways for carrier transport.

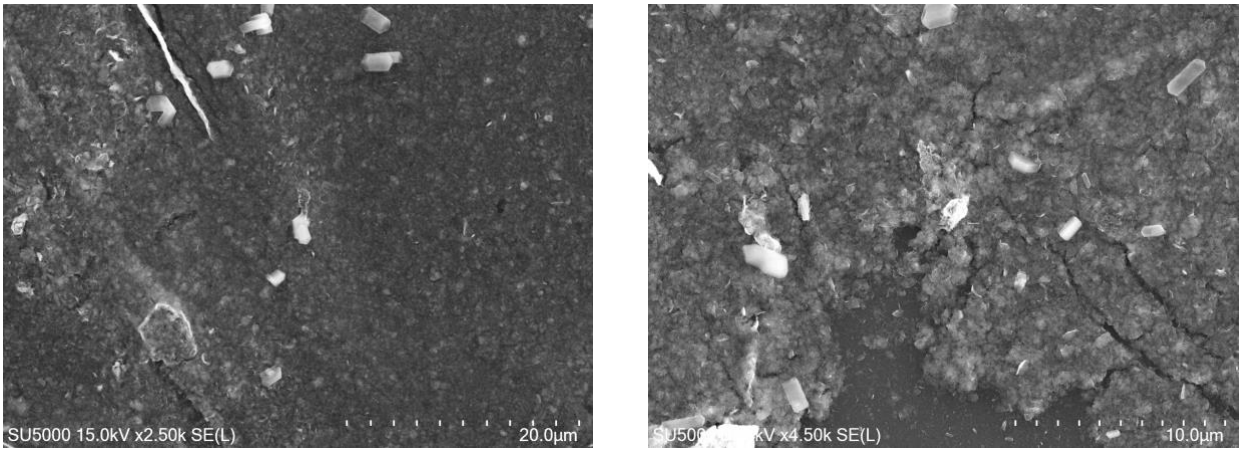

(a) (b)

Figure 2.8 a) and b) SEM images of rod-coated 100 mg/ml MoS_2 solution on 2 cm × 2 cm Si substrate using rod RDS #95 with 8 coats.

2.3.4 Surface treatment

There are two primary surface groups on Si/SiO_2 substrates: silanol groups (Si-OH) with high polarization and siloxane (Si-O-Si) groups with low polarization. [94] The presence of silanol groups leads to a hydrophilic surface due to the formation of hydrogen bonds between silanol groups and water molecules. In contrast, a SiO_2 surface with siloxane groups is hydrophobic because hydrogen bonds with water molecules are absent. However, both surface groups change over time to reduce the surface energy. Silanol groups adsorb water and hydrocarbons, while siloxane groups undergo rehydration, converting to silanol. Therefore, it is crucial to minimize the time duration between surface treatment and thin film deposition. Any treatments aimed at improving the hydrophilicity of Si/SiO_2 substrates should promote the formation of silanol groups on the SiO_2 surface. Common surface treatments of Si/SiO_2 substrates reported in the literature [94,95] include hydrofluoric acid (HF) dipping, potassium hydroxide (KOH) cleaning, piranha treatment and oxygen plasma treatment.

In this study, acetone, IPA and ethanol cleaning and piranha treatment followed by oxygen plasma treatment were investigated as two surface treatments to improve the wetting of MoS_2 dispersions with higher concentrations on Si/SiO_2 substrates. The experimental process of these two surface treatments has been described in detail in section 2.2.2. The impacts of these two surface treatments on the hydrophilicity of SiO_2 surface were quantitatively determined by measuring the contact angle of DI water on Si/SiO_2 substrates immediately after the surface treatment. For comparison, the contact angle of Si/SiO_2 substrates following standard cleaning procedure was also measured. Each surface treatment was conducted on four 2 cm × 2 cm Si/SiO_2 substrates. The contact angle of DI water was measured at 5 different locations of a single sample. The contact angle of an individual sample was the average of these five values and the contact angle for a specific surface treatment was the average of the contact angles of four samples undergoing the surface treatment. According to Table 2.1, Si/SiO_2 substrates that undergo piranha and O_2 plasma treatment have the smallest contact angle (10 ° - 20 °) among substrates prepared by the three different surface treatments. The contact angle of substrates cleaned by acetone, IPA, and DI water ranges from 20 ° to 30 °, while the contact angle of substrates cleaned by acetone, IPA and ethanol is between 30 ° and 40 °. According to the values of contact angle, hydrophilicity of the SiO_2 surface was enhanced by piranha and O_2 plasma treatment. However, the SiO_2 surface became less hydrophilic after it is cleaned by acetone, IPA, and ethanol.

During the rod coating process of MoS_2 flakes, it has been observed that the wetting of MoS_2 solution was improved on both substrates subject to these two surface treatments, evidenced by the dispersion spreading across a larger area of the substrate pretreated with either of these two treatments in contrast to a substrate that underwent standard cleaning. However, the wetting of MoS_2 dispersion on substrates treated by piranha and oxygen plasma seems to be better than the

counterpart cleaned by acetone, IPA, and ethanol. The improvement in the wetting MoS_2 solution on substrates cleaned by ethanol was suspected to be the result of the remaining ethanol residue on the SiO_2 surface. In addition to the wetting of MoS_2 dispersion, the enhancement in hydrophilicity of the substrate may also contribute to improved adhesion properties of the deposited film to the substrate.

Table 2-1 Contact angle of 2 cm × 2 cm Si/SiO_2 substrates following different surface treatments.

Surface Treatment	Standard Cleaning	Acetone/ IPA /Ethanol	Piranha Treatment/O_2 plasma
Average Contact Angle (°)	24.5	32.8	15.6
Standard Deviation (°)	3.0	4.7	1.5

2.3.5 Thermal annealing temperature

The purpose of thermal annealing is to evaporate the remaining solvent within the solution-processed film, thereby reducing the distance between overlapped flakes and boosting inter-flake physical and electrical connection. The solvent of MoS_2 solution is ethanol, whose boiling point is about 78.23 °C. Thus, the annealing temperature of rod-coated MoS_2 film needs to exceed the boiling temperature of ethanol. Apart from facilitating solvent evaporation, thermal annealing would also accelerate the slow desulfurization process of MoS_2. Siao et al. [96] have demonstrated that a higher temperature (annealing temperature: 110 °C) expedites the escape of sulfur atoms from the surface of mechanically exfoliated MoS_2 flakes, resulting in sulfur vacancies in MoS_2 and unintentional n-type doping of MoS_2. As a result, thermal annealing influences the electrical properties of MoS_2 film, indicated by the sheet resistance. At first, the sheet resistance of the samples was measured by Ossila four-point probe. But Ossila four-point probe did not provide any sheet resistance values. Instead, a second measurement setup consisting of a four-point probe connected to a Keithley 2400 Source Meter system was adopted. The reliability of the second measurement setup was first verified prior to assessing sheet resistance. Two previously prepared

samples (Number of coats: 8; MoS_2 solution concentration; 100 mg/ml; sample 1 surface treatment: piranha treatment; sample 2 surface treatment: acetone, IPA, ethanol cleaning) were selected as their sheet resistance could be evaluated by the first measurement setup. The measured values of these two samples by the second measurement setup were compared with those obtained from the first measurement setup for validation. It's worth noting that the sheet resistance measurement with the second measurement setup was conducted 3 or 4 months later than the measurement by the first measurement setup. It could be anticipated that the sheet resistance of these two samples would increase due to the adsorption of foreign molecules in air. The values shown in Table 2.2 are of the same order of magnitude, suggesting that the results obtained from the second measurement setup could be considered as an estimation of the actual sheet resistance. In Table 2.3, MoS_2 film annealed at 400 °C exhibits a far lower sheet resistance compared to films annealed at other temperatures. Hence, the optimal thermal annealing temperature of rod-coated MoS_2 film is 400 °C.

Table 2-2 Sheet resistance values of MoS_2 film on Si/SiO_2 substrates measured by the first and second measurement setup.

Sample	1st setup Average Rs (MΩ/□)	Standard Deviation (MΩ/□)	2nd setup Average Rs (MΩ/□)	Standard Deviation (MΩ/□)
1	47	10	73	17
2	54	12	228	135

Table 2-3 Sheet resistance values of MoS_2 on 1 cm × 1 cm Si/SiO_2 substrates annealed at different temperatures.

Annealing Temperature (°C)	150	200	300	350	400
Average Rs (Ω/□)	3.2×10^6	88×10^6	654×10^6	92×10^6	0.12×10^6
Standard Deviation (Ω/□)	0.45×10^6	0.57×10^6	145×10^6	13×10^6	0.13×10^6

2.4 Characterization of optimized MoS_2 Flake Film

The investigation of the impacts of film deposition parameters on the quality of prepared MoS_2 film led to the determination of coating parameters. A MoS_2 film was prepared on a 2 cm × 2 cm Si/SiO_2 substrate according to the following determined optimal rod coating procedure. The substrate was immersed in a 250 ml piranha solution with a volume ratio of sulfuric acid to hydrogen peroxide equal to 4 for 15 minutes, followed by a 10-minute oxygen plasma treatment in a plasma strip/descum system before the rod coating of MoS_2 flakes. MoS_2 solution with a concentration of 100 mg/ml was then deposited on a 2 cm × 2 cm Si/SiO_2 substrate immediately after its oxygen plasma treatment using a Mayer rod of number 95 to achieve 16 coats. The as-prepared film was thermally annealed at 400 °C in a rapid thermal processor for 30 minutes.

The surface coverage of flakes on the substrate and the morphology of the film was observed using SEM at 5 kV. In Figure 2.9, MoS_2 flakes deposited on the substrate have covered most of the area of the substrate surface, making it a suitable platform for developing microelectronics. However, one major issue with rod-coated MoS_2 film is its poor uniformity. Certain areas of the substrate exhibit a higher density of flakes than others. The uniformity of film is particularly compromised near the edges of the substrate, which is presumably caused by the presence of solution droplets at the edge and uneven pressure applied to the bar. In Figure 2.9 b-d, there are visible cracks on the deposited film, leaving some areas of the substrate not covered by MoS_2 flakes. In addition, flakes overlap on top of each other randomly, resulting in a rough surface. The electrical property of the MoS_2 film was evaluated by measuring its sheet resistance with the second measurement setup. Resistance values were obtained at 6 different positions on the sample and averaged to provide an area-averaged result. The optimized MoS_2 flake film demonstrated an average sheet resistance of 27 ± 6 kΩ/□. Film thickness measurement was conducted on samples

with 8 coats of MoS_2 flakes using both the profilometer and AFM prior to the measurement of the optimized film. Both measurements yield quite divergent values of film thickness, so no definite value of MoS_2 film thickness could not be drawn from these measurement results. The poor uniformity of MoS_2 film could be one contributing factor. In addition, removing film near the edge of the substrate to produce a step-like structure does not resolve in a sharp interface separating the film and substrate, further contributing to the inaccuracy of film thickness measurement. Therefore, film thickness was instead measured on photolithography defined MoS_2 channels in the fabricated MoS_2 TFTs. The fabrication process of channels is described in Chapter 3. The thickness of rod-coated MoS_2 film in this study falls within the range of 200 to 400 nm. Its resistivity is estimated to be between $(54 \pm 12) \times 10^{-2}$ Ω·cm and $(108 \pm 24) \times 10^{-2}$ Ω·cm. Lin and Su measured the resistivity of a CVD-grown MoS_2 film on a SiO_2/Si substrate with a thickness of approximately 3.3 nm in a Hall measurement, showing a resistivity value on the order of 10^{-3} Ω·cm at room temperature. [97]

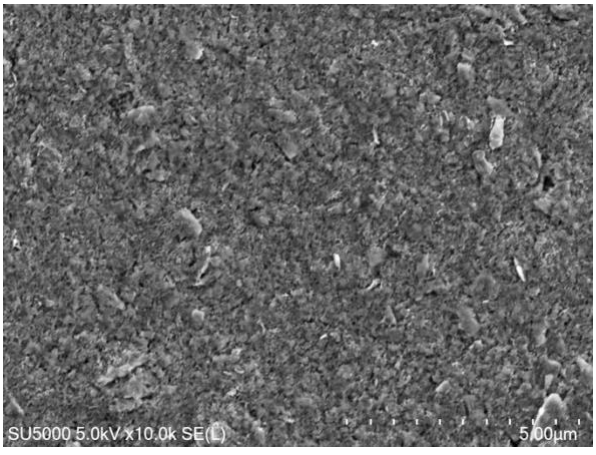

(a)

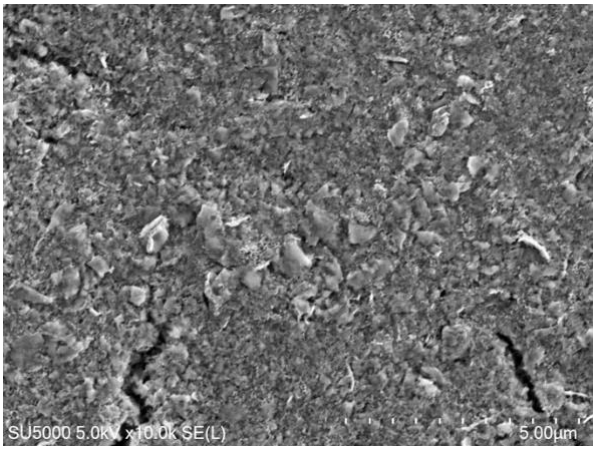

(b)

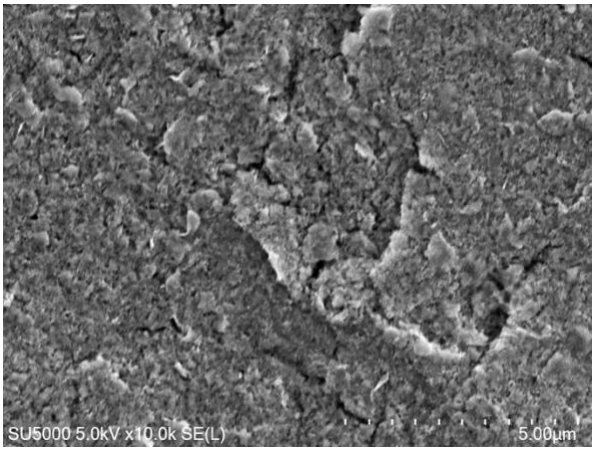

(c)

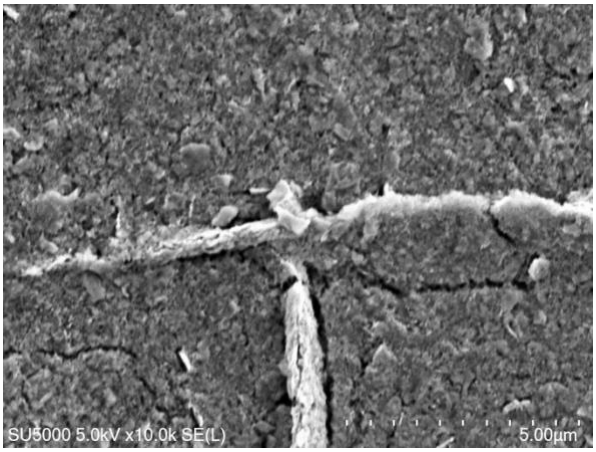

(d)

Figure 2.9 a-d SEM images of MoS_2 film deposited using the optimal coating parameters on a Si/SiO_2 substrate.

2.5 Conclusion

It was shown that rod coating can be used as a simple method to achieve electrically continuous films of MoS_2 flakes. The film thickness can be controlled through the Mayer rod wire thickness, solution concentration and number of coats. Given the relatively low concentrations of MoS_2 flakes in the solution, the optimal deposition of MoS_2 film was achieved by employing the highest coating parameters attempted: a Mayer rod of number 95, a 100 mg/ml MoS_2 solution, and a total of 16 coats. In theory, thicker films could be achieved by increasing these parameters, but Mayer rods with a rod number larger than 95 are generally not used, solutions with higher concentrations of flakes are likely to cause flake agglomeration, and the number of coats larger than 16 is impractical. Therefore, rod coating can only be used to deposit thin films. Of the annealing temperatures tested, 400 °C led to the lowest film resistance. Since this temperature was the highest tested, the effect of higher temperatures should be investigated, and possibly the effect of longer annealing times. The prepared film annealed at 400 °C exhibits an average sheet resistance on the order of kΩ/□, which is several orders of magnitude lower than the typical sheet

resistance values reported in the literature for a CVD-grown monolayer MoS_2 (10^5 – 10^6 Ω/□) [98, 99]. Its calculated resistivity is on the order of 10^{-1} Ω·cm, which is two orders of magnitude larger than a CVD-grown MoS_2 film reported in a previous study [97].

One problem that needs to be addressed is the poor uniformity of the rod-coated film. As the surface coverage increases, there are more flakes stacking on top of each other. Another contribution to the poor uniformity of the flake film is the remaining solution droplets near the edge of the substrate after the rod coating. This issue would be improved on a manufacturing scale when larger substrates are used, and when automated rod coating machines are employed which would have more uniform pressure along the bar compared to the hand-based coating method used here. The rod coating method could easily be applied to deposit other 2D flakes on silicon substrates or even flexible substrates such as polyethylene terephthalate (PET), offering an alternative approach for the deposition of large-area solution-processed 2D flake films.

Chapter 3 Device Integration of Rod-coated MoS_2 Films

3.1 Fabrication of MoS_2 – based Thin Film Transistor

3.1.1 Device Design

After depositing a nearly continuous MoS_2 film on a Si/SiO_2 substrate, thin film transistors (TFTs) based on MoS_2 thin film were fabricated. MoS_2 thin film served as the channel material and heavily p-doped silicon functioned as a back gate, as illustrated in Figure 3.1. The source and drain electrodes consisted of 50 nm of titanium and 150 nm of gold. The thickness of titanium, usually employed as a binding layer for the gold electrode, was intentionally set to a relatively considerable value. This decision stems from the fact that the Fermi level of titanium (the work function of 4.33 eV) closely aligns with the conduction band edge of monolayer MoS_2, which would facilitate the formation of an Ohmic contact. The dimensions of the semiconductor channel were on the order of microns as the continuous coverage of MoS_2 flakes was achieved on this scale according to the SEM images presented in Chapter 2. Variations in channel dimensions were incorporated into the design to explore the influence of channel dimensions on the source-to-drain current of the device. In instances where the channel width was held constant, a reduction in channel length was anticipated to increase the source-to-drain current because there would be fewer flake-to-flake contacts in the channel. The flake-to-flake contact is associated with junction resistance. The edges of flakes could be a source of scattering centers [100], thereby impeding the carrier transport through the channel. There should also be a rise in source-to-drain current with increasing channel width when the channel length remains the same. The enlarged cross-sectional area of a widened channel permits more charge carriers to pass through the channel. The electrical characterization of TFTs with different channel dimensions would test these hypotheses.

The channel lengths were designed to be 1.5 μm, 4 μm, or 10 μm, and the channel width was set to 5 μm, 10 μm, 15 μm or 20 μm. The channel dimensions were a combination of these 3 different channel length values and 4 different channel width values, leading to 12 distinct sizes of the channel. There would be 12 repeating units of a device with a specific combination of channel length and width, hence a 12 × 12 array of devices to investigate the effect of channel length and width on the electrical performance of the devices. The electrical characterization of devices would provide information on the field-effect mobility of carriers and enable the assessment of rod-coated MoS_2 as a channel material.

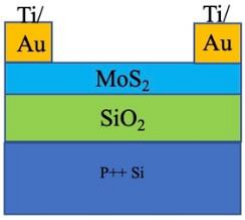

Figure 3.1 Cross-section schematic of MoS_2- based thin film transistor.

3.1.2 Device Fabrication

The fabrication process involves the following steps:

Step 1: Substrate cleaning and surface treatment

A 4-inch heavily p-doped silicon wafer with a layer of 300 nm thermally grown SiO_2 on top (University wafer, resistivity ranging from 0.001 to 0.005 Ω·cm) was cut into 2 cm × 2 cm pieces using a dicing saw (DAD3240, Disco Corporation). This process was described in detail in section 2.2.2. Four cross alignment marks of 200 nm gold were deposited on the periphery of the substrate by electron beam after the patterning by photolithography, the etching of SiO_2 via reactive ion etching of SF_6 and O_2, and the lift-off of the gold film by acetone with the assistance of ultrasonication.

The substrate was then cleaned with acetone, IPA, and DI water in an ultrasonication bath for 280 s each. To enhance the hydrophilicity of the SiO_2 surface, the substrate was immersed in a piranha solution with a sulfuric acid to hydrogen peroxide volume ratio of 4:1 for 15 minutes, followed by rinsing in 3 consecutive DI water baths for 2 minutes each. After, the substrate was treated with oxygen plasma (flow rate: 50 sccm; RF power: 500 w; pressure: 800 mTorr) for 10 minutes to activate the surface before the coating of MoS_2 flakes.

Step 2: Rod coating of MoS_2 flakes and thermal annealing

A Mayer rod with a number 95 (RDS specialties) was used to coat MoS_2 dispersion in ethanol at a concentration of 100 mg/ml on the substrate for 16 coats. The film near the edge of the substrate was removed by acetone every 4 coats to reveal the alignment marks deposited on the substrate. It was observed that the area of the substrate covered by MoS_2 flakes exhibited better wetting of MoS_2 solution compared to bare SiO_2 surface, resulting in a denser coverage of MoS_2 flakes in the center region of the substrate. Two deposited MoS_2 films were thermally annealed at 300 °C and 400 °C with argon in a rapid thermal processor, respectively. The average sheet resistance of MoS_2 film annealed at 300 °C was measured as 764 ± 117 MΩ/□ using the second sheet resistance measurement setup, which was approximately three orders of magnitude higher than its counterpart annealed at 400 °C (average sheet resistance: 91 ± 5 kΩ/□).

Step 3: Patterning of MoS_2 channel by photolithography

Two different negative photoresists, ma-N 1410 (micro resist technology) and AZ nLOF 2035 (Integrated Micro Materials), were spin coated onto 300 °C and 400 °C annealed MoS_2 films, respectively. The photoresist layers were baked at 100 °C and 110 °C for one minute separately, with expected thickness of 1 μm and 3 μm. The channels were patterned onto MoS_2 films through photolithography using a maskless aligner (MLA 150, Heidelberg Instruments) with a laser

wavelength of 375 nm. The dose values for these two photoresists were 75 mJ/cm^2 and 80 mJ/cm^2 respectively. The depth of focus value was set to -2 for both photoresists. After exposure, photoresist AZ nLOF 2035 was baked at 115 °C for one minute. The rationale behind selecting two different negative photoresists stemmed from the objective of comparing their effectiveness in shielding the underlying MoS_2 film from etching species during the reactive ion etching process for the isolation of channel elements until etching species removed the parts of MoS2 film not covered by the photoresist.

Step 4 Reactive ion etching of MoS_2 film

Once the photoresist had been developed in the corresponding developer solution and dried by nitrogen, MoS_2 films with photoresist on top were etched by chlorine gas and oxygen in a reactive ion etching system (ICP380, Oxford Instruments) (Recipe: Cl_2 flow rate: 30 sccm; O_2 flow rate: 10 sccm; RF Power: 200 W). Although SF_6 is a common etching species [102-104] for MoS_2 flakes, it would also etch the SiO_2 layer underneath [105]. MoS2 film with photoresist ma-N 1410 on top was etched for 6 minutes as some of the photoresist patterns had been removed during this period. According to the optical microscope image in Figure 3.2, it appears that MoS_2 film exposed to etching species was completely etched away after a 6-minute etching. The etching duration of MoS_2 film with photoresist AZ nLOF 2035 on top was 23 minutes. Similar to the previous case, some of the photoresist was removed. Although Cl_2 does not react with SiO_2 chemically, the thickness of the SiO_2 layer underneath was still reduced after this extended etching duration. The problem with this fabrication step was that channels were not completely isolated. Subsequently, the remaining photoresist was removed by oxygen plasma in a plasma photoresist strip/descum system.

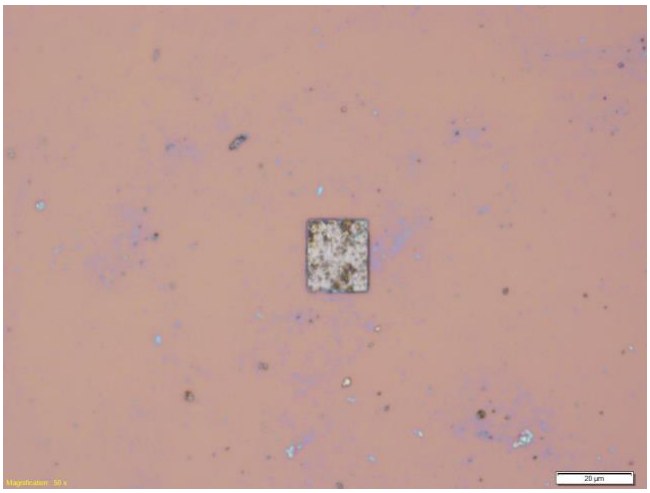

Figure 3.2 Optical microscope image of the first row and twelfth column element of 300 °C annealed MoS_2 film. The scale bar is 20 μm.

Step 5 Patterning of electrode by photolithography

A bilayer positive photoresist of PMGI SF7 (Kayaku) and Shipley 1811 (Microposit) was subsequently spin coated on top of the sample with a spin speed of 4000 rpm and 3000 rpm, respectively. The soft bake was conducted at 170 °C and 115 °C for 90 seconds each. The patterning of electrodes was achieved by photolithography, using a laser of 405 nm with a dose of 75 mJ/cm^2 and depth of focus of -2, followed by the development of photoresist in MF-319 developer solution for 45 seconds.

Step 6 Deposition of metal electrodes through E-beam

Metal electrodes, consisting of 50 nm titanium and 150 nm gold, were deposited onto the sample via electron beam evaporation (Angstrom Engineering Amod Electron Beam Evaporator) with a deposition rate of 3 angstroms/s for titanium and 1.5 angstroms/s for gold. The thickness of the titanium binding layer was increased to reduce the Schottky barrier between the metal electrodes and MoS_2 channel because the Fermi level of titanium (-4.33 eV) is close to the conduction band edge of monolayer MoS_2. In the following, a lift-off process was performed by

immersing samples in a remover PG solution (Kayaku) heated to 80 °C for 20 minutes and subsequent cleaning in IPA and DI water. A problem encountered in the process was that some MoS_2 channel elements were washed off from the substrate surface, resulting in a low yield of devices. One approach to address this issue is to use a metal shadow mask for the e-beam deposition of metal electrodes after the etching of MoS_2. Noteworthily, more channel elements were remaining on the 400 °C annealed MoS_2 sample than its 300 °C annealed counterpart. It seems that thermal annealing at 400 °C also enhances the adhesion of flake film to the substrate. Consequently, an additional thermal annealing process at 400 °C prior to electrode patterning may improve the device yield.

Step 7 Annealing of metal/MoS_2 contact

To improve the contact between MoS_2 film and metal electrodes, fabricated field-effect transistors based on MoS_2 were annealed at 400 °C under an argon atmosphere in a rapid thermal processor for 15 minutes. Optical microscope images of TFTs based on 400 °C annealed MoS_2 film are shown in Figure 3.3.

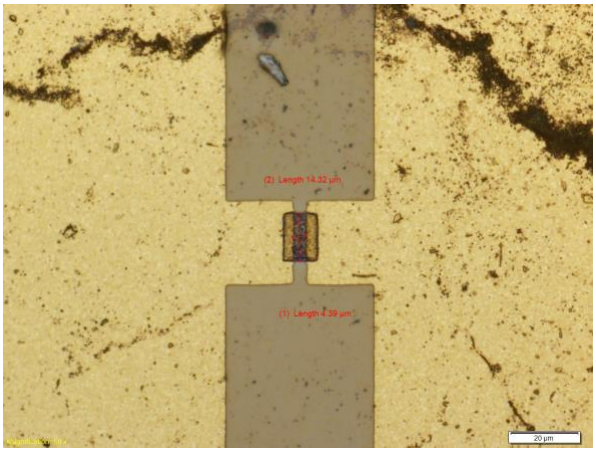

(a)

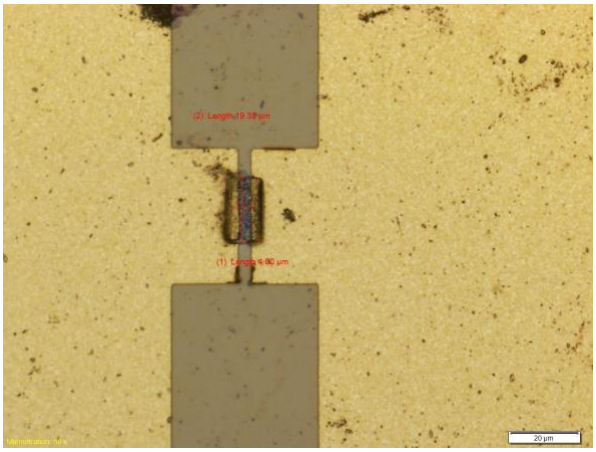

(b)

Figure 3.3 Microscope images of a) 11-7 and b) 4-8 channel element of 400 °C annealed MoS_2 film. The scale bar is 20 μm.

3.1.3 Measurement of channel thickness

As stated in section 2.4, the measurement of film thickness by removing film near the edge of the substrate could not yield reliable results due to the non-uniformity of rod-coated film and unintentional thinning of film at the borderline. Photolithography, on the other hand, provided a sharp interface between MoS_2 film and the substrate, enabling a more accurate determination of flake film thickness. However, it should be noted that the incomplete removal of MoS_2 film between channels would lead to an underestimation of the actual film thickness.

The dimensions of the channel elements were measured using an optical microscope (MX-61A, Olympus). The values of the channel length and width were summarized in Table 3.1. The film thickness of a channel was measured by an atomic force microscope (AFM) (Dimension fast scan, Bruker), with a scan size of either 5 μm or 10 μm. As the AFM tip scanned horizontally across the surface of the sample during the measurement, the top and bottom edges of the channel were aligned perpendicular to the tip. The channel thickness was measured either from the top edge or the bottom edge with two different scan sizes. Based on the AFM measurement results in Table 3.2, the thickness of 300 °C annealed MoS_2 film was between 100 and 200 nm, with average surface roughness (R_a) ranging from 30 to 70 nm. In light of the average surface roughness values obtained from AFM measurements, the thickness of the titanium layer of the metal electrodes should be increased to 100 nm in future work to ensure complete coverage of the MoS_2 film underneath, while the gold layer of metal electrodes should be set to 100 nm. Further evidence of film non-uniformity could be observed in AFM images shown in Figure 3.4.

Table 3-1 The values of channel length and width of 300 °C annealed MoS_2 film and the deviation percentage from their designed values.

Channel Element Numbering	Length (μm)	Design length (μm)	Deviation Percentage (%)	Width (μm)	Design Width (μm)	Deviation Percentage (%)
1-7	3.48	4	-13	14.71	15	-1.93
1-12	9.8	10	-2	19.74	20	-1.3
4-8	3.74	4	-6.5	19.87	20	-0.65
7-12	9.8	10	-2	19.74	20	-1.3
10-7	3.87	4	-3.25	14.71	15	-1.93

Table 3-2 Film thickness of 300 °C annealed MoS_2 film measured by AFM.

Channel Element Numbering	Bottom edge Thickness (nm)	Top edge thickness (nm)	Average Thickness (nm)	R_a (nm)
1-7	212	187	199.5	65.75
1-12	106	144	125	54.1
4-8	159	120	139.5	59.95
7-12	90.9	88.2	89.55	36.85
10-7	130	168	149	56.3

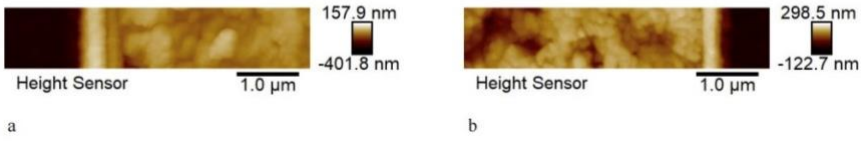

Figure 3.4 AFM images of a) 1-7 and b) 4-8 MoS_2 channel elements.

The measurement of channel length and width under an optical microscope was repeated for MoS_2 annealed at 400 °C. The values were presented in Table 3.2. AFM measurement of

channel thickness was also conducted. Unlike the previous case, the AFM images did not show a clear borderline between the channel and the substrate, making it difficult to measure the channel thickness. Several scan sizes had been attempted, including 5, 10, and 20 μm. The MoS_2 film was expected to be thicker than in the previous case since in this sample there was better coverage of MoS_2 flakes on the channel. There had been attempts to measure the thickness of channels with a profilometer (DektakXT, Bruker), but precise control of the probe to scan across the channel was challenging because of the microscale size of the channels. Instead, the thickness of a cross alignment mark composed of MoS_2 film located close to channels of TFT was measured with a scan size of 800 μm, which provided an estimation of the channel thickness. Three different positions of the alignment mark were measured by the profilometer and summarized in Table 3.3. Accordingly, the thickness of channels could be estimated to be between 200 nm and 400 nm with an average surface roughness ranging from 50 nm to 100 nm. The thickness measurement of MoS_2 film annealed at both 300 °C and 400 °C has revealed a relatively significant surface roughness, which could be caused by the poor uniformity of rod coated flake film and reactive ion etching (RIE) for device isolation.

Table 3-3 The values of channel length and width of 400 °C annealed MoS_2 film and the deviation percentage from their designed values.

Channel Element Numbering	Length (μm)	Design length (μm)	Deviation Percentage (%)	Width (μm)	Design Width (μm)	Deviation Percentage (%)
1-8	3.87	4	-3.25	19.74	20	-1.3
1-10	9.8	10	-2	8.64	10	-13.6
2-6	3.48	4	-13	9.93	10	-0.7
2-9	9.8	10	-2	4.26	5	-14.8

2-10	9.93	10	-0.7	6.97	10	-30.3
4-8	4	4	0	19.35	20	-3.25
4-9	9.55	10	-4.5	4.77	5	-4.6
4-12	9.93	10	-0.7	19.61	20	-1.95
5-9	9.68	10	-3.2	5.03	5	0.6
5-10	9.68	10	-3.2	10.32	10	3.2
6-10	9.93	10	-0.7	10.19	10	1.9
6-11	9.93	10	-0.7	14.58	15	-2.8
8-6	4	4	0	9.8	10	-2
8-8	3.87	4	-3.25	18.96	20	-5.2
8-10	9.68	10	-3.2	9.93	10	-0.7
10-6	4.13	4	3.25	9.93	10	-0.7
11-7	4.39	4	9.75	14.32	15	-4.53

Table 3-4 Film thickness of cross alignment mark on 400 ℃ annealed MoS_2 film measured by a profilometer.

Position	Thickness (nm)	R_a (nm)
1	239.28	94.04
2	263.48	53.66
3	227.66	68.45

3.2 Electrical Characterization of Device

3.2.1 $I_d - V_d$ Characteristics

Electrical characterization of MoS_2-based TFTs was conducted by a semiconductor 4200A-SCS parameter analyzer and Everbeing probe station in dark at ambient conditions. Two-terminal characterization was performed to measure the variation of source-to-drain current (I_d) with applied bias voltage (V_d), where a bias voltage was applied between the source and drain

electrode. As the bias voltage swept from -10 V to 10 V and subsequently in reverse (from 10 V to -10 V), there was a hysteresis on the current-voltage plot (Figure 3.5) of TFTs based on MoS_2 film annealed at 300 °C independent of the size of the channel. The hysteresis was also observed in TFTs based on 400 °C annealed MoS_2 film regardless of the length and width of the channel, which may indicate the presence of trap states in the channel originating from grain boundaries of MoS_2 flakes [67], adsorption of foreign molecules in the air on the surface of MoS_2 [106] and the interface between MoS_2 film and SiO_2.

The $I_d - V_d$ characteristics demonstrated a non-linear relation. The current-voltage plot was basically symmetric around the origin, with some exceptions. S-shaped $I_d - V_d$ characteristics were also reported for TFTs based on a solution-processed MoS_2 film deposited via spray coating with a thickness of 200 nm [67]. The non-ohmic behavior evidenced by the s-shaped $I_d - V_d$ characteristics could be attributed to contact resistance between the metal electrodes and the channel or weak inter-flake connections. Zeng et al. [67] claimed that weak inter-flake connection was the limiting factor for the channel conductivity as the contact resistance obtained from a transmission line measurement was insignificant when compared to the channel resistance. This statement was supported by the agreement between the experimental data and simulation results of a thermionic emission model between two adjacent flakes [67]. The relation between source-to-drain current and bias voltage of three TFTs with different channel lengths and widths was plotted in the same figure (Figure 3.6). It was observed that the current flowing through a shorter channel was higher than a longer channel with a comparable width, which was consistent with the expected behavior. Figure 3.7 plots the $I_d - V_d$ characteristics of four TFTs based on the 400 °C annealed MoS_2 film, demonstrating as expected that the current in a channel with a larger width was higher than in a narrower channel with a similar length. However, the conjecture of improved electrical

performance of a shortened channel did not manifest in MoS_2 TFTs annealed at 400 °C. The discrepancy between the assumption mentioned in section 3.1.1 and the results obtained from TFTs based on MoS_2 film annealed at 300°C or 400 °C was possibly due to the complication of contacts between adjacent flakes in the channel.

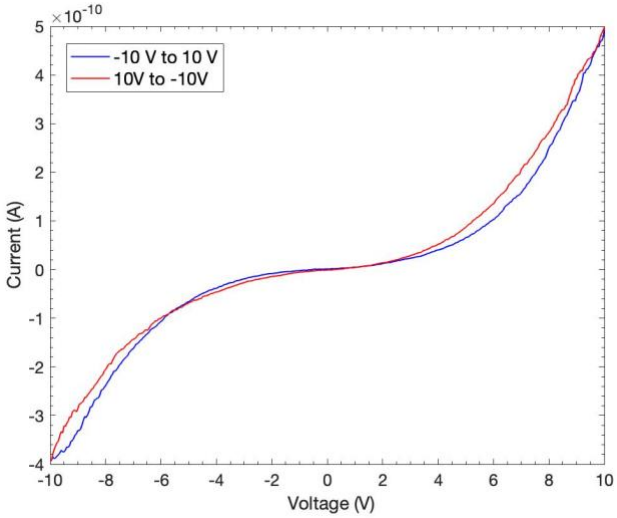

Figure 3.5 Hysteresis of a 300 °C annealed MoS_2 film-based thin film transistor with a channel length of 3.48 μm and a channel width of 14.71 μm.

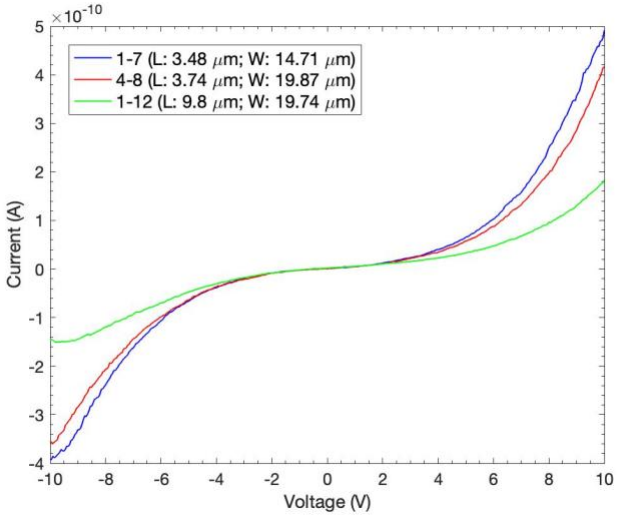

Figure 3.6 $I_d - V_d$ characteristics of three thin film transistors based on the 300 °C annealed MoS_2 film.

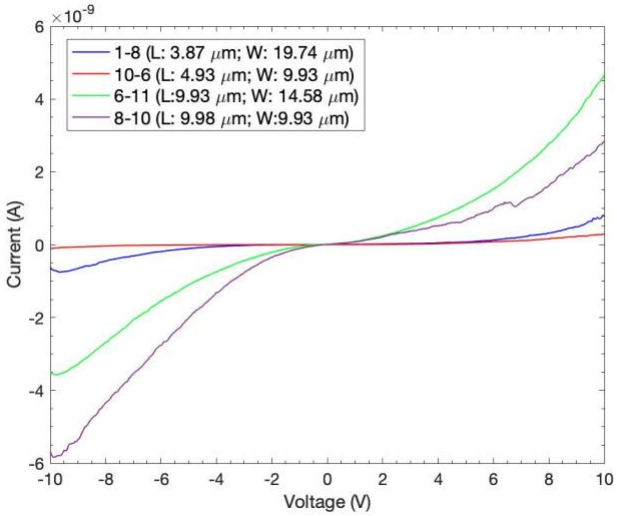

Figure 3.7 $I_d - V_d$ characteristics of four thin film transistors based on 400 °C annealed MoS_2 film.

3.2.2 $I_d - V_g$ Characteristics

The SiO_2 layer was scratched by a diamond scribe to be connected to the probe as a back gate in the three-terminal characterization. A piece of glass was placed under the sample to prevent the heavily p-doped silicon substrate from being grounded by the probe station holder. A fixed bias voltage was applied between the source and drain electrode, while the gate electrode was applied with a linear voltage sweep from -50 V to 50 V. According to Figure 3.8, there was not any significant gate modulation effect observed in the three-terminal characterization of TFTs based on MoS_2 films annealed at both 300 °C and 400 °C, which was not in line with previously reported n-type behaviour of FETs based on either a MoS_2 flake [107,108] or a solution-processed MoS_2 film [56, 67]. Multiple factors could have contributed to the absence of a gate effect in FETs based on rod-coated MoS_2 film including the property of rod-coated MoS_2 film, dielectric interface, and contact resistance. As a solution-processed film, there could be defects and surface traps in the MoS_2 film prepared by rod coating, thereby diminishing the efficiency of the gate effect. Adsorbates of oxygen and water molecules in air on the surface of MoS_2 could introduce

trap states and interfere with the gating effect. The inhomogeneity of the MoS_2 film may also play a part. If the MoS_2 film is too thick, it might not respond well to the applied gate voltage. Regarding the dielectric interface, the adsorbates present at the SiO_2 interface also introduce defects and trap states consequently leading to charge trapping and scattering, which reduces the effectiveness of the gate modulation. Another influential factor is contact resistance. High contact resistance between metal and MoS_2 would lead to poor carrier injections, and hence a reduced gate effect.

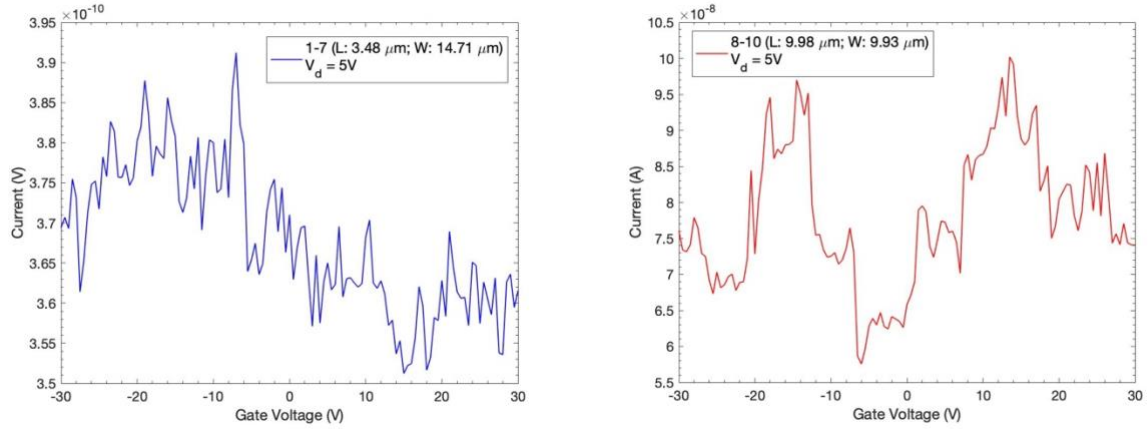

(a) (b)

Figure 3.8 I_d – V_g characteristics of a) 1-7 element of 300 °C annealed and b) 8-10 element of 400 °C annealed MoS_2 thin film transistor.

An alternative approach to investigate the gate effect of rod coated MoS_2 film is conducting a capacitance–gate voltage measurement of a metal-oxide-semiconductor (MOS) capacitor based on MoS_2 film. A schematic of the proposed MoS_2-based MOS capacitor is shown in Figure 3.9. The thin film transistor structure introduced in this chapter could be utilized for such a measurement by connecting a probe to one electrode and a second probe to the back gate. However, the overlap between the electrode and the MoS_2 channel might not provide a substantial overlapping area, potentially limiting the achievable performance. MoS_2 MOS capacitors could also be fabricated separately. The fabrication process of a MoS_2 MOS capacitor is comparatively less complex than a TFT, requiring only the patterning and deposition of metal electrodes

subsequent to the rod coating of MoS_2 flakes. The device exhibits the structure of an inverted MOS capacitor, with a heavily p-doped silicon substrate acting as the top gate and a Ti/Au electrode serving as the back contact. The gate effect could be demonstrated by a transition between the accumulation regime and depletion regime of capacitance as the gate voltage varies.

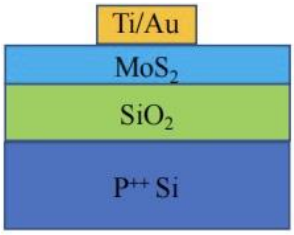

Figure 3.9 Cross-section schematic of a MoS_2 MOS capacitor.

3.3 Conclusion

MoS_2 thin-film TFTs were fabricated, exhibiting a non-ohmic behaviour in two-terminal characterizations due to weak contacts between adjacent flakes. However, there was not any significant gate effect of the MoS_2 channel observed in three-terminal characterizations. Potential causes for the absence of gate modulation effect include incomplete isolation of devices and a relatively thick gate layer compared to the channel width. An alternative approach to verify the gate effect of MoS_2 film is to measure the capacitance-voltage relation of the MOS capacitor based on MoS_2 film.

Chapter 4 Silver Nanowire Transparent Electrode for WS_2–Based LEDs

4.1 Introduction

2D materials have garnered significant attention from the research community due to their unique properties and potential for developing next-generation electronic and optoelectronic devices. Among them, monolayers of transition metal dichalcogenides (TMDCs) such as MoS_2, $MoTe_2$, WS_2 and others show promise for optoelectronic applications as a result of their direct bandgap in the visible to near-infrared range. In this chapter, transparent LEDs are fabricated. Transparent LEDs are of interest for new applications like see-through displays, smart windows, or head-up displays. The high optical transparency and mechanical flexibility of TMDCs resulting from their atomic thickness make them ideal for applications in transparent and flexible devices. For a transparent LED, there is an additional material requirement that needs to be addressed - the top transparent electrode.

Transparent electrodes are thin films of materials that possess both optical transparency and electrical conductivity. They are integral components in a variety of electronic and optoelectronic devices, including solar cells, organic light-emitting diodes (OLEDs), touch screens and transparent heaters. LEDs based on 2D or organic materials are typically deposited on a film of indium tin oxide (ITO), the most commonly used transparent electrode material. After the deposition of the active layers of the LED, a second electrode on top is fabricated typically by evaporating a thin coating of metal such as silver or aluminum, which is opaque. For a transparent LED, however, this top electrode needs to be transparent. ITO requires sputtering at high temperature and pressure for deposition, which damages the underlying 2D or organic materials. Thus, an alternative material is needed for this top electrode.

Silver nanowires have been touted as a promising transparent electrode material to replace ITO. It consists of randomly oriented meshes of nanowires which form a conductive network without covering the whole surface, such that light can pass through. The silver nanowires are most often synthesized in solution, and then deposited on substrates through simple deposition methods like spin coating [110], spray coating [111] and Mayer rod coating [112]. Deposition can take place in ambient conditions and thus cause far less damage to the layers underneath than the deposition of ITO. Silver nanowire transparent electrodes have similar transparency and conductivity values as ITO while having the additional advantage of being highly mechanically flexible [109].

In collaboration with Professor Tilmar Kümmell's group at University Duisburg-Essen in Germany, a transparent light emitting device based on monolayer WS_2 was developed by employing transparent electrodes on both sides of a vertical architecture. Hole transport layers (HTLS) were spin coated on pre-patterned ITO on a glass substrate, followed by transfer of metal-organic vapour deposition (MOCVD)-grown WS_2 as the active material. The direct deposition of zinc oxide (ZnO) as an electron transport layer (ETL) was achieved through the atmospheric-pressure spatial atomic layer deposition (AP-SALD) process. A silver nanowire network was integrated as a transparent top contact through spin coating. The design, fabrication, and characterization of the device were carried out by Henrik Myja in Professor Tilmar Kümmell's group. My involvement was solely in the preparation of silver nanowire electrodes. This work led to a paper in the journal *Nanotchnology* [113], which section 4.3 draws heavily on.

4.2 Silver Nanowire Film Deposition and Characterization

Prior to the integration of silver nanowires as the cathode in WS_2-based transparent LEDs, a silver nanowire network is prepared on a glass substrate. Pre-cleaned Fisherbrand premium plain glass microscope slides were cut into 1.5 x 1.5 cm pieces using a diamond scribe. Two different deposition methods were tested to determine which was more suitable: rod coating and spin coating. Ultralong silver nanowire with a nominal diameter of 30 nm dispersed in ethanol with a concentration of 20 mg/mL was purchased from Novarials Corporation (Woburn, MA). Silver nanowire dispersion with a lower concentration could be prepared by diluting the original solution in a glass vial.

The performance of a transparent electrode is determined by its transmittance and sheet resistance. A UV-Vis spectrometer (Shimadzu UV 2550) equipped with an integrating sphere was utilized to measure the transmittance of the silver nanowire network on glass substrates and fabricated devices. The measurement data was subsequently corrected by the transmittance of a blank glass substrate. The sheet resistance measurement was measured with an Ossila four-point probe. The maximum current flowing through the outer two probes was set to 10 mA and the voltage between the inner two probes was measured 25 times on 9 different positions of the silver nanowire film to provide a time and area-averaged result.

4.2.1 Rod Coating

The process of fabricating a silver nanowire network by Mayer rod coating is described as follows. First, glass substrates were cleaned with acetone, IPA, and DI water in an ultrasonication bath for 90 s each, followed by drying with an N_2 air gun. Then, diluted silver nanowire solution in a glass vial was shaken by hand for 5 minutes to improve the dispersion of silver nanowires

because silver nanowires agglomerate over time. Ultrasonication to improve silver nanowire dispersion was not conducted due to the possibility of nanowire breakage. 20 μL of silver nanowire solution was pipetted along one edge of the substrate evenly. A Mayer rod (RDS 10, RD Specialities) with a wire diameter of 0.25 mm was gently rolled across the substrate with even speed and pressure. The substrate was rotated 90° counterclockwise and the silver nanowire dispersion was shaken for another 1 minute ahead of the next coating. This process was repeated until coating had been conducted along each of the 4 edges of the substrate. The prepared samples were thermally annealed in a vacuum oven at 150 ºC for 30 minutes to enhance the contact between silver nanowires and reduce the sheet resistance [114]. This annealing temperature and duration were previously found in our group to minimize the sheet resistance for 30 nm diameter silver nanowires [114].

Silver nanowire solutions with different concentrations, ranging from 0.3 mg/mL to 1.0 mg/ml, were deposited on glass substrates using the rod coating method to investigate the impact of nanowire density on transmittance and sheet resistance of the resulting nanowire film. Four samples at each concentration were prepared. In this subsection and the next subsection, the optical transmittance of prepared samples was measured by a window tint meter (SRW 2000) at 550 nm. To determine the transmittance of the silver nanowire network, the measured values were divided by the transmittance of a blank glass substrate. This calculation yields specular or direct transmittance, which only takes into account the transmitted light travelling in the same direction as the incident light. This value does not include the diffusive transmittance, which represents the transmitted light scattered by the subject. Since the diffuse transmittance is excluded, the total transmittance of the silver nanowire network is expected to be larger than the specular transmittance. The specular transmittance and sheet resistance values of these four samples were

measured and then averaged as well as summarized in Table 4.1 below. As expected, an increase in the concentration of silver nanowire solution leads to a decline in both the transmittance and sheet resistance of the silver nanowire film. A higher density of silver nanowires provides more conductive paths for current transport, thereby lowering the sheet resistance. However, an increasing number of silver nanowires also results in greater reflectance and scattering of the incident light, hence scaling down transmittance. Like other materials used for transparent electrodes, there is a trade-off between optical transmittance and electrical conductivity.

Table 4-1 Transmittance and sheet resistance of rod-coated silver nanowire film on glass.

AgNW Concentration (mg/ml)	Average Specular Transmittance (%)	Average Sheet Resistance (Ω/□)
1	80.0	9.3
0.7	81.3	11.5
0.6	81.9	14.0
0.5	84.5	17.1
0.4	85.5	19.8
0.3	87.9	21.8

4.2.2 Spin Coating

Spin coating is a film deposition method in which a solution of the desired material in a solvent is cast onto a spinning substrate to produce a thin film. The centrifugal force generated by the spinning motion spreads the solution evenly over the substrate's surface, forming a uniform thin film. In this study, the static dispensing technique was employed to deposit silver nanowire solution onto a glass substrate instead of dynamic dispensing. 40 μL of silver nanowire dispersion was dropped onto the substrate. The spin speed was set to 1500 rpm and the time duration was 60

seconds. Subsequently, the spin-coated silver nanowire film is dried under UV light (DentMate TRAYDEX18) immediately after the first coat, and the process was repeated for a second coat. Afterwards, a thermal annealing process was conducted at 150 ^{0}C in a vacuum oven for 30 minutes. This process is depicted in Figure 4.1.

Silver nanowire solutions with two distinct concentrations were prepared to determine the optimal concentration for the performance of silver nanowire electrodes. Two samples were fabricated for each distinct concentration. Table 4.2 below presents the transmittance and average sheet resistance values of silver nanowire film fabricated using dispersions of 1 mg/ml and 2 mg/ml. Like rod-coated films, the trade-off between transmittance and sheet resistance exists. In comparison with rod coating, silver nanowire films deposited by spin coating have a desirably lower sheet resistance at a given transparency. The SEM image (Figure 4.2) reveals some alignment of silver nanowires, as well as the formation of circular nanowires. Based on the values provided in the table, a silver nanowire solution with a concentration of 2 mg/ml appears to be suitable for the spin coating process as the resulting film possesses a sheet resistance below 10 Ω/□ without significantly comprising its transmittance (transmittance > 80 %).

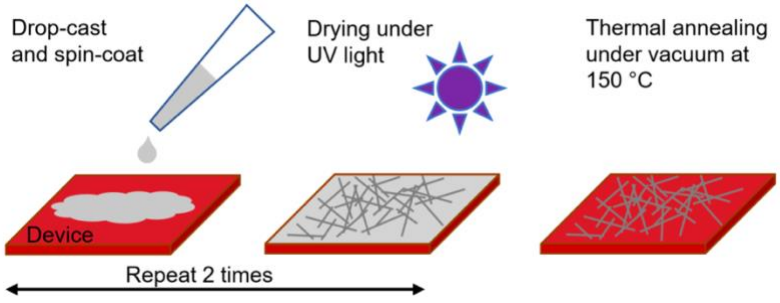

Figure 4.1 Schematic of the spin-coating process to deposit silver nanowire network [113].

Table 4-2 Transmittance and sheet resistance of spin-coated silver nanowires on glass.

AgNW Concentration (mg/ml)	Specular Transmittance (%)	Average Sheet Resistance (Ω/□)

1	85.2	11.2
2	80.9	9.1

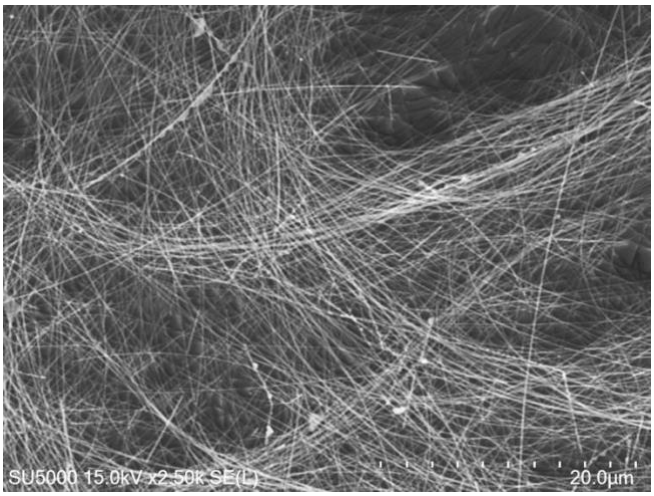

Figure 4.2 SEM image of spin-coated 2 mg/ml 30 nm silver nanowires on a glass substrate.

4.2.3 Silver Nanowire Electrode Characterization

Spin coating was selected as the method to deposit silver nanowires as the transparent top contact in this work to prevent potential damage to the active material in the device resulting from the pressure exerted by the Mayer rod. And, as seen above, the transparency and resistance values are similar to or better than the rod-coated electrodes. A nanowire concentration of 2 mg/ml was selected since a sheet resistance below 10 Ω/□ was desired. For comparative purposes, the silver nanowire network was also prepared on a blank glass substrate (sample 1 and 2) following the identical procedure employed for the device.

In Figure 4.3a, the as-prepared silver nanowire film on glass exhibits small yet discernible dots which are agglomerates of silver nanowires. The morphology of the silver nanowire network was characterized by scanning electron microscopy (SEM) at 1 kV. It is evident from the SEM imaging (Figure 4.2 and 4.3b) that silver nanowires intersect with each other to develop a network.

The average length of the silver nanowires was measured to be 88 μm ± 39 μm based on the measurement of 40 nanowires and the average diameter of 49 μm ± 15 μm was determined from 64 nanowires. The distribution is shown in Figure 4.4. These dimension statistics are provided by my groupmate Muhammed Kayaharman. The transmittance of sample 1 and 2 across the visible range (380 -750nm) is shown in Figure 4.3c. The average transmittance across this wavelength range is 77% ± 2% and 74% ± 1%, respectively. These transmittance values are lower than the value shown in Table 4.2 because the transmittance value in Table 4.2 was measured at 550 nm whereas here it is an average across the whole visible spectrum. The feature shown on the transmittance spectrum between 300 nm and 400 nm is attributed to surface plasmon resonance, which is commonly observed in silver nanowire films [116-118].

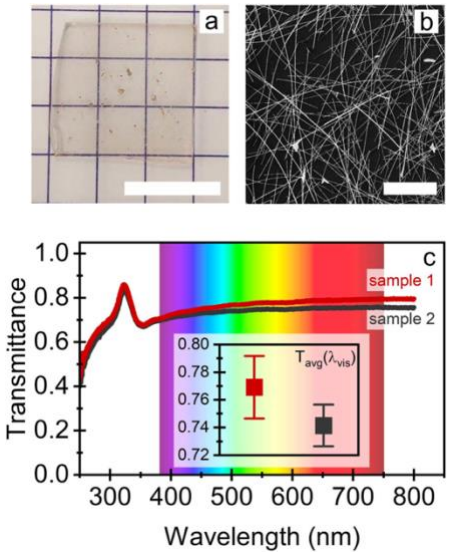

Figure 4.3 (a) Photo of silver nanowire film on the glass. The scale bar is 1 cm. (b) SEM image of the silver nanowire network on silicon. The scale bar is 20 μm. (c) Spectral transmittance (corrected for glass substrate) of two silver nanowire films on glass. The inset shows the average transmittance for the entire visible spectrum [113].

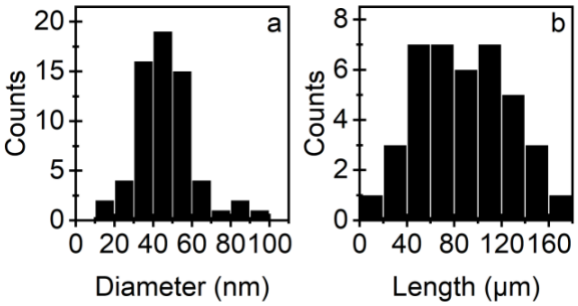

Figure 4.4 Silver nanowire a) diameter and b) length distribution as determined from SEM images [113].

4.3 WS_2 LED Results and Discussion

A schematic and photograph of the WS_2–based LED is shown in Figure 4.5a and b. The devices are composed of poly(3,4-ethylene dioxythiophene) polystyrene sulfonate (PEDOT: PSS) and poly[N, N'-bis(4-butylphenyl)-N, N'-bisphenylbenzidine] (poly-TPD) as combined hole transport layers (HTLs) spin-coated on ITO-coated glass from VisionTec Systems Ltd. (layer thickness of 150 nm, sheet resistance of 15 Ω/□ and surface roughness around 1 nm). An MOCVD-grown monolayer WS_2 is the active material, the electron transport layer (ETL) consists of ZnO deposited via AP-SALD, and silver nanowire electrodes were applied through spin coating. Details of the fabrication can be found in our paper [113]. A cross-sectional SEM image was captured at a breaking edge of the fabricated device, facilitating the evaluation of individual layer thickness (Figure 4.6). The estimated thickness of ITO, combined HTLs and ZnO is 140 nm, 75 nm, and 40 nm, respectively. On a fabricated sample measuring 1.5 cm × 1.5 cm, there are 6 LEDS with an emission area of approximately 6 mm^2. The emission area is defined by the overlap between pre-patterned ITO and layers of materials shaped into rectangles by mechanically removing all material layers between individual LEDs. According to the transmittance spectrum (Figure 4.5c), the devices exhibit an average transmittance of 63% ± 10% in the visible spectral range. The substrate causes a reduction in transmittance in the ultraviolet range, as demonstrated by the transmittance

spectrum of the ITO/glass substrate. Furthermore, poly TPD and ZnO contribute to additional absorption below ~ 420 nm.

The WS_2-based LED fabricated with AP-SALD ZnO deposited at 150 ^{0}C emits red light with a peak wavelength of 650 nm and a full width at half maximum (FWHM) of around 42 nm when subjected to a bias voltage of 7 V and a resulting current density of 0.5 A cm^{-2}. In Figure 4.7 (a), the current density of the WS_2-based LED shows a non-linear increase from 0.1 to 0.6 A cm^{-2} within the voltage of 2 V to 7 V. The turn-on voltage of the device is defined as the voltage at which a luminance of 10^{-4} cd m^{-2} is reached. The turn-on voltage of the device using AP-SALD ZnO deposited at 150 ^{0}C is 2.9 V. The device attains a luminance of 10^{-2} cd m^{-2} at 5V, while a maximum luminance of 8.8×10^{-2} cd m^{-2} is measured at 7V and 1.1 A cm^{-2} (Figure 4.7b). The electroluminescence (EL) spectra collected from both sides of the device depicted in Figure 4.8 yield comparable results, indicating that the device functions as a transparent LED with bidirectional emission. The low internal quantum efficiency (~ 10^{-4}) of MOCVD-grown WS_2 is a factor limiting the device's performance. High defect density in TMDCs grown via MOCVD [119-121] limits the quantum yield due to non-radiative recombination [122], as evidenced by defect-related emission revealed in low-temperature PL analysis [123]. In addition, the absence of charge balance in the active region severely impacts the device's performance, as it enhances non-radiative recombination and leads to carrier spillover [124].

To investigate the impact of the silver nanowire contact on device performance, devices utilizing spin-coated ZnO quantum dots as the ETL were fabricated with a typical aluminum thin-film top contact (which is opaque and thus does not lead to a transparent LED) as well as a silver nanowire contact (Figure 4.9a). In Figure 4.10(b), the EL spectrum of the device with the silver nanowire contact at a bias voltage of 7 V is comparable to its counterpart with aluminum contact

at 5 V, both with a peak wavelength of ~ 650 nm. Despite exhibiting a comparable current density to its counterpart with aluminum contact, the device with silver nanowire contact does not display a rectifying behaviour (Figure 4.10a). At a bias voltage of 7 V, a maximum luminance of 1.8×10^{-2} cd m^{-2} is observed. However, the luminance and external quantum efficiency (EQE) of the device with the silver nanowire contact in Figure 4.10 (c) and (d) is one order of magnitude lower than its counterpart with aluminum contact. Although the integration of silver nanowires as the cathode yields a functional transparent LED, it suffers from lower efficiency and lack of emission homogeneity when compared to a device with an aluminum contact. Inhomogeneous emission might be a consequence of localized conduction paths through the device due to the random distribution of silver nanowires, which could potentially be addressed by the inclusion of an additional current spreading layer or the improvement of homogeneity on silver nanowire distribution through process adjustments. Another challenge associated with the silver nanowire electrode is its degradation in atmospheric conditions on a time scale of months.[125] The stability of the silver nanowire network can be enhanced through effective passivation. Various passivation materials have been proposed in previous studies, including organic molecules (MUA [126], TPPA [127], photoresist [128], PFSA [129]), metal oxide (ZnO [130], ZnO/Al_2O_3 [131], TiO_2 [132]) and reduced graphene oxide [110]. Storing the device in a nitrogen atmosphere is also beneficial for preserving its functionality, as supported by the EL spectra (Figure 4.8) measured one year after the device was fabricated.

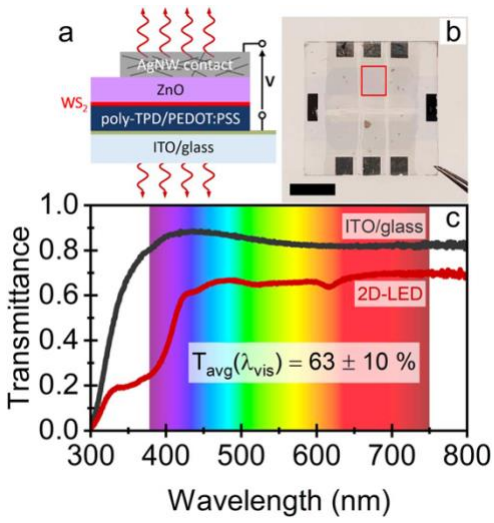

Figure 4.5 (a) Schematic of device architecture of WS2–based LED. (b) Photo of fabricated WS_2–based LEDs. The red rectangle delineates the emitting area of one device. (c) Spectral transmittance of a 2D-LED (red) and a glass substrate covered with ITO (black) [113].

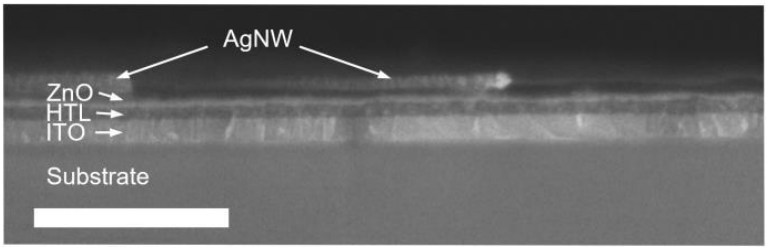

Figure 4.6 Cross-sectional SEM image of WS_2 - based LED. The scale bar has dimensions of 1 μm in length and 100 nm in width [113].

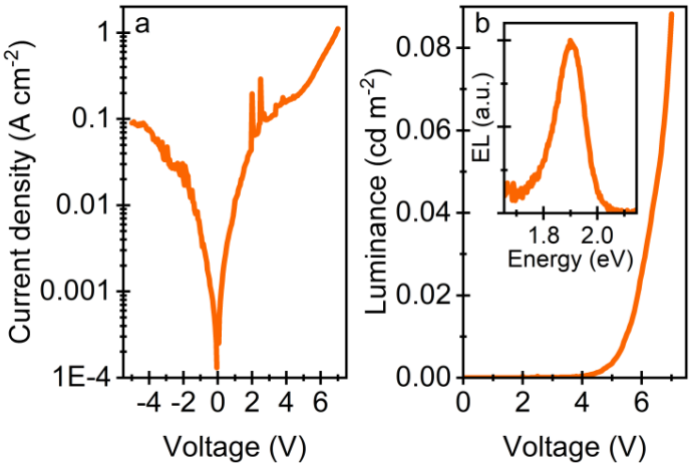

Figure 4.7 Photometric measurements of the brightest transparent LED (150 ^{0}C AP-SALD ZnO). a) Plot of current density versus voltage. b) Luminance measured at positive voltages and (inset) an EL spectrum at 7V and 0.5 A cm $^{-2}$ [113].

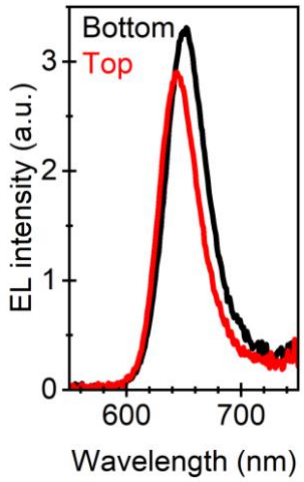

Figure 4.8 EL spectra collected from the substrate side (black) and top contact side (red) of the transparent LED fabricated with AP-SALD ZnO at 150 °C [113].

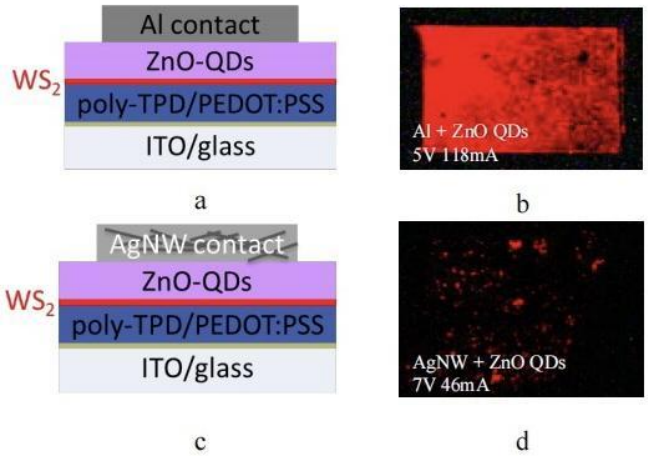

Figure 4.9 a) and b) Schematic and electroluminescence of a WS_2-based LED with an aluminum contact. c) and d) Schematic and electroluminescence of a WS_2-based LED with a silver nanowire electrode.

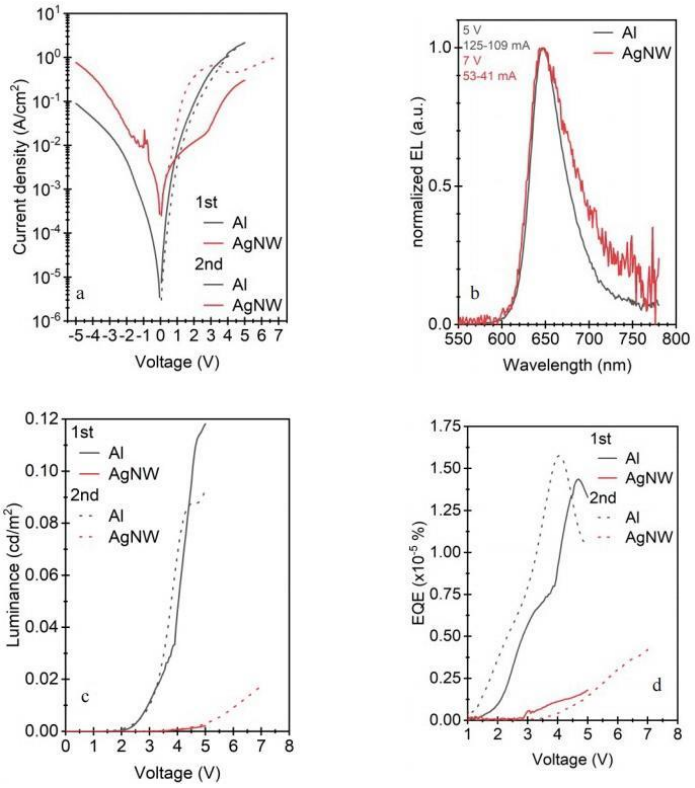

Figure 4.10 a) Current density versus voltage, b) normalized EL spectrum, c) luminance versus voltage and d) external quantum efficiency versus voltage of devices with aluminum and silver nanowire contacts.

4.4 Conclusion

Two thin film deposition methods, spin coating and Mayer rod coating, have been applied to deposit a random network of silver nanowires on glass substrates. Each method possesses distinct advantages and limitations. Mayer rod coating is a scalable method which could be adopted in the industry for roll-to-roll production. It is also a versatile technique that is not only suitable for rigid substrates like silicon and glass but also for flexible substrates such as PET. In terms of film quality, Mayer rod coating facilitates the formation of a silver nanowire network with acceptable transmittance in the visible range and sheet resistance using a nanowire dispersion at relatively low concentrations. However, this method does result in the presence of a small number of stripes in the film and could damage underlying layers due to the need for the rod to make

physical contact with the sample. Spin coating appears to strike a better balance between transmittance and sheet resistance and likely causes less damage to underlying layers. However, it has the drawbacks of being less scalable, and results in more wastage of nanowires, compared to the rod-coating method.

The silver nanowire network was integrated as a top contact of a transparent LED based on MOCVD-grown WS_2 in a vertical device architecture. A two-step spin coating process was employed to deposit a silver nanowire network with sheet resistance comparable to that of ITO and an absolute transmittance of nearly 80% over the visible range. Although a reasonable luminance was achieved, further optimization is still needed. Regarding the silver nanowire electrodes, enhancement in the homogeneity and uniformity of the network should be pursued, alongside the consideration of passivation strategies to improve their stability.

Chapter 5 Summary and Future Work

5.1 Conclusion

In this study, monolayer MoS_2 flakes dispersed in ethanol were deposited on Si and Si/SiO_2 substrates using the Mayer rod coating method. This marks the first instance in which the Mayer rod coating method has been employed to deposit a thin film of transition metal dichalcogenides. Multiple factors influence the quality of the prepared film, including the concentration of MoS_2 dispersion, Mayer rod number, number of coats, annealing temperature, and hydrophilicity of the substrate surface. The surface coverage of flakes on the substrate can be improved by increasing the concentration of MoS_2 solution, the Mayer rod number, and the number of coats. A sequential treatment of piranha followed by oxygen plasma was implemented to improve the hydrophilicity of the SiO_2 surface which in turn promoted wetting of the MoS_2 flakes. The electrical transport property of the flake film is affected by the thermal annealing temperature. Thermal annealing of rod-coated films was conducted at temperatures ranging from 150 to 400 °C. There was a significant decrease in the sheet resistance of MoS_2 film when annealed at 400 °C, whereas films annealed at other temperatures exhibited sheet resistances that were orders of magnitude higher. Further investigation into annealing temperatures exceeding 400 °C would provide a more comprehensive understanding of the relation between the sheet resistance of the film and annealing temperature. Applying a Mayer rod of number 95 to deposit 100 mg/ml MoS_2 solution on Si/SiO_2 substrates for 16 coats and subsequent thermal annealing at 400 °C for 30 minutes yields the optimal MoS_2 film with sheet resistance on the order of kΩ/□.

Rod coating presents a promising alternative to the deposition methods of solution-processed 2D materials reported in the literature. To the best of the author's knowledge, rod coating had only been employed to deposit graphene and its derivatives (graphene oxide). This

study has demonstrated that the rod coating method could be applied to deposit dispersions of other 2D materials. The rod coating method possesses several advantages. The first is its scalability. This method could be adopted in the industry for roll-to-roll production. In addition, the operation of rod coating is simple and cost-effective, and can be performed under ambient conditions. Moreover, it is suitable for depositing 2D flakes on a variety of substrates, including rigid substrates like glass and silicon, as well as flexible substrates such as polyethylene terephthalate (PET). Therefore, there is no need for an extra transfer process, as seen in vacuum filtration. On the other hand, some challenges were encountered during the rod coating of MoS_2 flakes. The primary difficulty lies in achieving uniformity. The deposition may get less dense as the rod is rolled across the substrate, which is usually compensated by multiple coats in orthogonal directions. This issue of uniformity is expected to improve if the rod coating were performed on larger substrates, with the use of an automated rod coating machine, and upon other optimizations that would be performed were this scaled to manufacturing levels. The viscosity of the solution could also affect the uniformity as a dispersion with higher viscosity ink tends to ball up rather than spread evenly on the substrate. Future work on proper ink formulation should be of great help. It was found that rod coating is appropriate for thin films on the order of 100 nm. Thick films are not possible as it is not realistic to increase the rod number, the concentration of flakes in the solution nor the number of coats. Even if the uniformity problem were solved, the deposition of monolayer film through rod coating would also be difficult, unlike with Langmuir Blodgett, as multiple layers are required to obtain overlapping flakes needed for an electrically continuous film. However, rod coating could be used for sub-monolayer films if a certain density of isolated flakes is needed for an application.

Thin film transistors based on as-prepared MoS_2 film were fabricated, with MoS_2 serving as the channel material and heavily p-doped silicon substrate as the back gate. The source-to-drain current of the device exhibited a non-linear relation with the applied bias voltage, indicating non-ohmic behaviour. The weak inter-flake connection is suspected to be the limiting factor of the electrical performance of the device. However, the applied gate voltage exerts negligible control over the current flowing through the channel. It is clear that future work is needed to improve the electrical connection between overlapping flakes.

In Chapter 4, the Mayer rod coating method was applied to deposit silver nanowires on glass substrates, showcasing the versatility of this film deposition method. The network of silver nanowires was integrated with a LED based on monolayer WS_2 as a transparent electrode, enabling bidirectional emission and demonstrating the functionality of a transparent LED. Despite a reasonable luminance of 8.8×10^{-2} cd/m^2 achieved at 7 V, further improvement is still needed. The device with a silver nanowire electrode showed reduced efficiency and inhomogeneous emission compared to its counterpart with an aluminum contact. The inhomogeneity of emission could be caused by the random conductive pathways in the silver nanowire network, requiring efforts to improve the uniformity of the network. The stability of the silver nanowire network is another issue that needs to be addressed. This can likely be solved by coating the nanowires with an encapsulation layer such as polyurethane, which is a transparent polymer which has been shown to provide effective passivation [135].

5.2 Future Work

One of the primary focuses for future work will be to develop an approach to improve the uniformity of MoS_2 film deposited by the Mayer rod coating method. To address this issue, the

use of a Mayer rod with a larger wire diameter may prevent the MoS_2 solution from getting trapped inside the grooves of the rod during the rod coating process, thus aiding the deposition of a more uniform film. Other surface treatments, such as KOH cleaning, HF dipping and reoxidation via high-temperature annealing, could be performed to provide a better understanding of how the hydrophilicity or hydrophobicity of SiO_2 surface affects the uniformity of the solution-processed film. Once a rod-coated film with improved uniformity is achieved, conducting Hall measurement on the deposited film could provide information on the type of major charge carrier, carrier concentration and mobility. Other work regarding the property of deposited film is to measure the contact resistance between two overlapping flakes and investigate how it is affected by thermal annealing and ageing.

Substantial efforts should be directed at enhancing the performance of field effect transistors based on MoS_2 thin film. To start with, the etching recipe should be modified to achieve complete isolation of MoS_2 channels. One suggestion is to replace chlorine gas with xenon disulfide (XeF_2) as the etching gas in the reactive ion etching process. Similar to Cl_2, XeF_2 does not react with SiO_2 chemically. A previous study has reported that MoS_2 flakes with a thickness of less than 300 nm could be completely removed by XeF_2 at a pressure of 1 Torr within 4 minutes. [133] The short etching duration of XeF_2 could reduce the possibility of thinning the SiO_2 layer due to ion bombardment. Additionally, it is advisable to encapsulate the MoS_2 channel with insulating material at the end of the fabrication process to prevent the adsorption of water and oxygen molecules in the air. One suitable candidate is PMMA. Zeng et al. [67] discovered that a PMMA encapsulation layer also improves the contact between flakes in a solution-processed MoS_2 film by applying mechanical pressure to the channel, thereby improving the electrical performance of a TFT [67]. Aside from enhancing the flake-flake contact by annealing or reducing inter-flake

distance, the addition of molecules chemically bonding adjacent flakes should also be considered. π-conjugated dithiolated molecule 1,4-benzene dithiol ($C_6H_6S_2$) has been added to drop-casted MoS_2 film, which not only heals the sulfur vacancies in the MoS_2 film but also forms covalent bonds to bridge adjacent flakes [134]. After the performance of the TFT is optimized, its function as a photodetector should be illustrated by characterizing the spectral response range, responsivity, detectivity and response time. There should also be an investigation into the stability of the device in ambient conditions.

In the forthcoming research regarding silver nanowire electrodes, a focus will be placed on the improvement of their performance. Challenges associated with silver nanowire electrodes manifest in two aspects, the presence of localized conductive paths within silver nanowires and the gradual degradation of silver nanowires over time. Localized conductive paths in the transparent electrode are hypothesized to stem from the random distribution of silver nanowires. The alignment of silver nanowires or the incorporation of a current spreading layer is likely to address this issue. In comparison with spin coating, the application of rod coating is more likely to induce the alignment of silver nanowires perpendicular to the Mayer rod due to hydrodynamic force. Cho et al. [136] achieved a cross-aligned silver nanowire network through rod coating polyvinylpyrrolidone (PVP)-capped silver nanowire dispersion on a substrate pretreated with amine group terminated poly-L-lysine (PLL), which can be attributed to the combination of shear-induced hydrodynamic force and electrostatic interaction between negatively charged PVP-capped silver nanowires and positively charged amine groups. The long-term durability of silver nanowire electrodes could be enhanced via the passivation of silver nanowires. In the literature, there have been attempts to passivate silver nanowires by coating an additional layer of organic molecules (e.g. TPPA [127], photoresist [128], PFSA [129]) or reduced graphene oxide [110], as well as

functionalization of silver nanowires with organic molecules like MUA [126]. Moreover, the deposition of metal oxides such as ZnO [130], ZnO/Al_2O_3 [131] and TiO_2 [132] on top of silver nanowires could also protect silver nanowires from oxidization. Following the optimization of silver nanowires electrodes, silver nanowire networks can be deposited as both cathode and anode of a LED on a flexible substrate to achieve a flexible and transparent LED.

References

1. Chang Chien, C. S., Chang, H. M., Lee, W. T., Tang, M. R., Wu, C. H., & Lee, S. C. (2017). *AIP Advances*, *7*(8).
2. Xu, H., Zhang, H., Guo, Z., Shan, Y., Wu, S., Wang, J., ... & Zhou, P. (2018). *Small*, *14*(48), 1803465.
3. Pak, Y., Park, W., Mitra, S., Sasikala Devi, A. A., Loganathan, K., Kumaresan, Y., ... & Roqan, I. S. (2018). *Small*, *14*(5), 1703176.
4. Nasr, J. R., Simonson, N., Oberoi, A., Horn, M. W., Robinson, J. A., & Das, S. (2020). *ACS nano*, *14*(11), 15440-15449.
5. Liu, B., Chen, L., Liu, G., Abbas, A. N., Fathi, M., & Zhou, C. (2014). *ACS nano*, *8*(5), 5304-5314.
6. Zhao, J., Li, N., Yu, H., Wei, Z., Liao, M., Chen, P., ... & Zhang, G. (2017). *Adv. Mater*, *29*(34), 1702076.
7. Novoselov, K. S., Geim, A. K., Morozov, S. V., Jiang, D. E., Zhang, Y., Dubonos, S. V., ... & Firsov, A. A. (2004). *science*, *306*(5696), 666-669.
8. Coleman, J. N., Lotya, M., O'Neill, A., Bergin, S. D., King, P. J., Khan, U., ... & Nicolosi, V. (2011). *Science*, *331*(6017), 568-571.
9. Butler, S. Z., Hollen, S. M., Cao, L., Cui, Y., Gupta, J. A., Gutiérrez, H. R., ... & Goldberger, J. E. (2013). *ACS nano*, *7*(4), 2898-2926.
10. Gupta, A., Sakthivel, T., & Seal, S. (2015). *Progress in Materials Science*, *73*, 44-126.
11. Hu, G., Kang, J., Ng, L. W., Zhu, X., Howe, R. C., Jones, C. G., ... & Hasan, T. (2018). *Chemical Society Reviews*, *47*(9), 3265-3300.

12. Anasori, B., Xie, Y., Beidaghi, M., Lu, J., Hosler, B. C., Hultman, L., ... & Barsoum, M. W. (2015). *ACS nano*, *9*(10), 9507-9516.

13. Naguib, M., Mochalin, V. N., Barsoum, M. W., & Gogotsi, Y. (2014). *Advanced materials*, *26*(7), 992-1005.

14. Anasori, B., Lukatskaya, M. R., & Gogotsi, Y. (2017). *Nature Reviews Materials*, *2*(2), 1-17.

15. Dean, C. R., Young, A. F., Meric, I., Lee, C., Wang, L., Sorgenfrei, S., ... & Hone, J. (2010). *Nature nanotechnology*, *5*(10), 722-726.

16. Hui, F., Pan, C., Shi, Y., Ji, Y., Grustan-Gutierrez, E., & Lanza, M. (2016). *Microelectronic Engineering*, *163*, 119-133.

17. Li, L. H., Santos, E. J., Xing, T., Cappelluti, E., Roldán, R., Chen, Y., ... & Taniguchi, T. (2015). *Nano letters*, *15*(1), 218-223.

18. Li, Q., Chen, L., Gadinski, M. R., Zhang, S., Zhang, G., Li, H. U., ... & Wang, Q. (2015). *Nature*, *523*(7562), 576-579.

19. Ferrari, A. C., Bonaccorso, F., Fal'Ko, V., Novoselov, K. S., Roche, S., Bøggild, P., ... & Kinaret, J. (2015). *Nanoscale*, *7*(11), 4598-4810.

20. Naguib, M., Mochalin, V. N., Barsoum, M. W., & Gogotsi, Y. (2014). *Advanced materials*, *26*(7), 992-1005.

21. Shen, P. C., Lin, Y., Wang, H., Park, J. H., Leong, W. S., Lu, A. Y., ... & Kong, J. (2018). *IEEE Transactions on Electron Devices*, *65*(10), 4040-4052.

22. Zhang, J., Wang, F., Shenoy, V. B., Tang, M., & Lou, J. (2020). *Materials Today*, *40*, 132-139.

23. Hao, W., Marichy, C., & Journet, C. (2018). *2D Materials*, *6*(1), 012001.

24. Vishwanath, S., Liu, X., Rouvimov, S., Mende, P. C., Azcatl, A., McDonnell, S., ... & Xing, H. G. (2015). *2D Materials*, *2*(2), 024007.

25. Zhan, L., Wan, W., Zhu, Z., Shih, T. M., & Cai, W. (2017, June). In *Journal of Physics: Conference Series* (Vol. 864, No. 1, p. 012037). IOP Publishing.

26. Chen, M. W., Kim, H., Ovchinnikov, D., Kuc, A., Heine, T., Renault, O., & Kis, A. (2018). *npj 2D Materials and Applications*, *2*(1), 2.

27. Voevodin, A. A., Waite, A. R., Bultman, J. E., Hu, J., & Muratore, C. (2015). *Surface and Coatings Technology*, *280*, 260-267.

28. Wang, J., Jiang, Z., Chen, H., Li, J., Yin, J., Wang, J., ... & Ruan, S. (2017). *Optics Letters*, *42*(23), 5010-5013.

29. Wang, J., & Liu, B. (2019). *Science and Technology of Advanced Materials*, *20*(1), 992-1009.

30. Stankovich, S., Dikin, D. A., Piner, R. D., Kohlhaas, K. A., Kleinhammes, A., Jia, Y., ... & Ruoff, R. S. (2007). *carbon*, *45*(7), 1558-1565.

31. Hu, G., Albrow-Owen, T., Jin, X., Ali, A., Hu, Y., Howe, R. C., ... & Hasan, T. (2017). *Nature communications*, *8*(1), 278.

32. Harvey, A., Boland, J. B., Godwin, I., Kelly, A. G., Szydłowska, B. M., Murtaza, G., ... & Coleman, J. N. (2017). *2D Materials*, *4*(2), 025054.

33. Paton, K. R., Varrla, E., Backes, C., Smith, R. J., Khan, U., O'Neill, A., ... & Coleman, J. N. (2014). *Nature materials*, *13*(6), 624-630.

34. Karagiannidis, P. G., Hodge, S. A., Lombardi, L., Tomarchio, F., Decorde, N., Milana, S., ... & Ferrari, A. C. (2017). *ACS nano*, *11*(3), 2742-2755.

35. Joseph, A. M., Nagendra, B., Bhoje Gowd, E., & Surendran, K. P. (2016). *Acs Omega*, *1*(6), 1220-1228.

36. Zhi, C., Bando, Y., Tang, C., Kuwahara, H., & Golberg, D. (2009). *Advanced materials*, *21*(28), 2889-2893.

37. Tang, Q., & Zhou, Z. (2013). *Progress in materials science*, *58*(8), 1244-1315.

38. O'Neill, A., Khan, U., & Coleman, J. N. (2012). Preparation of high concentration dispersions of exfoliated MoS2 with increased flake size. *Chemistry of Materials*, *24*(12), 2414-2421.

39. Cai, X., Luo, Y., Liu, B., & Cheng, H. M. (2018). Preparation of 2D material dispersions and their applications. *Chemical Society Reviews*, *47*(16), 6224-6266.

40. Ma, R., & Sasaki, T. (2010). *Advanced materials*, *22*(45), 5082-5104.

41. Cai, X., Ma, R., Ozawa, T. C., Sakai, N., Funatsu, A., & Sasaki, T. (2014). *Nanoscale*, *6*(23), 14419-14427.

42. Shen, J., Pei, Y., Dong, P., Ji, J., Cui, Z., Yuan, J., ... & Ye, M. (2016). *Nanoscale*, *8*(18), 9641-9647.

43. Lin, J. Y., Chan, C. Y., & Chou, S. W. (2013). *Chemical communications*, *49*(14), 1440-1442.

44. Diba, M., Fam, D. W., Boccaccini, A. R., & Shaffer, M. S. (2016). *Progress in Materials Science*, *82*, 83-117.

45. Li, M., Muralidharan, N., Moyer, K., & Pint, C. L. (2018). *Nanoscale*, *10*(22), 10443-10449.

46. Mosconi, D., Giovannini, G., Jacassi, A., Ponzellini, P., Maccaferri, N., Vavassori, P., ... & Garoli, D. (2019). *ACS omega*, *4*(5), 9294-9300.

47. Li, X., Zhang, G., Bai, X., Sun, X., Wang, X., Wang, E., & Dai, H. (2008). *Nature nanotechnology*, *3*(9), 538-542.

48. Cote, L. J., Kim, F., & Huang, J. (2009). *Journal of the American Chemical Society*, *131*(3), 1043-1049.

49. Osada, M., & Sasaki, T. (2012). *Advanced Materials*, *24*(2), 210-228.

50. Wang, C., Osada, M., Ebina, Y., Li, B. W., Akatsuka, K., Fukuda, K., ... & Sasaki, T. (2014). *ACS nano*, *8*(3), 2658-2666.

51. Xu, L., Tetreault, A. R., Khaligh, H. H., Goldthorpe, I. A., Wettig, S. D., & Pope, M. A. (2018). *Langmuir*, *35*(1), 51-59.

52. Zhao, T., Wang, R., Li, L., & Jiao, T. (2023). *Nano Futures*.

53. Yamaguchi, H., Eda, G., Mattevi, C., Kim, H., & Chhowalla, M. (2010). *ACS nano*, *4*(1), 524-528.

54. Kim, J. W., Kang, D., Kim, T. H., Lee, S. G., Byun, N., Lee, D. W., ... & Shin, H. S. (2013). *ACS nano*, *7*(9), 8082-8088.

55. Matsuba, K., Wang, C., Saruwatari, K., Uesusuki, Y., Akatsuka, K., Osada, M., ... & Sasaki, T. (2017). *Science advances*, *3*(6), e1700414.

56. Lin, Z., Liu, Y., Halim, U., Ding, M., Liu, Y., Wang, Y., ... & Duan, X. (2018). *Nature*, *562*(7726), 254-258.

57. Gascho, J. L., Costa, S. F., Recco, A. A., & Pezzin, S. H. (2019). *Journal of Nanomaterials*, *2019*, 1-12.

58. Park, M. J., Gravelsins, S., Shin, D. H., Hong, B. H., & Dhirani, A. A. (2021). *ACS Applied Nano Materials*, *4*(3), 3087-3094.

59. Li, H., Song, Z., Zhang, X., Huang, Y., Li, S., Mao, Y., ... & Yu, M. (2013). *Science*, *342*(6154), 95-98.

60. Li, J., Lemme, M. C., & Östling, M. (2014). *ChemPhysChem*, *15*(16), 3427-3434.

61. Carey, T., Cacovich, S., Divitini, G., Ren, J., Mansouri, A., Kim, J. M., ... & Torrisi, F. (2017). *Nature communications*, *8*(1), 1202.

62. Worsley, R., Pimpolari, L., McManus, D., Ge, N., Ionescu, R., Wittkopf, J. A., ... & Casiraghi, C. (2018). *Acs Nano*, *13*(1), 54-60.

63. Sui, X., Rangnekar, S. V., Lee, J., Liu, S. E., Downing, J. R., Chaney, L. E., ... & Chen, J. (2023). *Advanced Materials Technologies*, 2301288.

64. Li, J., Ye, F., Vaziri, S., Muhammed, M., Lemme, M. C., & Östling, M. (2013). *Advanced materials*, *25*(29), 3985-3992.

65. McManus, D., Vranic, S., Withers, F., Sanchez-Romaguera, V., Macucci, M., Yang, H., ... & Casiraghi, C. (2017). *Nature nanotechnology*, *12*(4), 343-350.

66. Hempel, M., Nezich, D., Kong, J., & Hofmann, M. (2012). *Nano letters*, *12*(11), 5714-5718.

67. Zeng, X., Hirwa, H., Metel, S., Nicolosi, V., & Wagner, V. (2018). *Solid-State Electronics*, *141*, 58-64.

68. Lobo, K., Thakur, R., Prasad, S. K., & Matte, H. R. (2022). *Journal of Materials Chemistry C*, *10*(48), 18326-18335.

69. Kim, K. W., Kim, J. H., Cho, S., Shin, K., & Kim, S. H. (2017). *Thin Solid Films*, *632*, 50-54.

70. Li, Z., Zhang, X., Shen, L., Fan, Z., Chen, X., Chen, M., ... & Chen, Q. (2019). *Journal of Coatings Technology and Research*, *16*, 1773-1780.

71. Zeng, L., Chen, S., Liu, M., Cheng, H. M., & Qiu, L. (2019). *ACS applied materials & interfaces*, *11*(50), 46776-46782.

72. Qi, X., Li, X., Jo, H., Bhat, K. S., Kim, S., An, J., ... & Lim, S. (2020). *Sensors and Actuators A: Physical*, *301*, 111697.

73. Wang, J., Liang, M., Fang, Y., Qiu, T., Zhang, J., & Zhi, L. (2012). *Advanced Materials*, *24*(21), 2874-2878.

74. Yang, Y., Liu, Z., Yin, Z., Du, Z., Xie, L., Yi, M., ... & Huang, W. (2014). *RSC Advances*, *4*(98), 55671-55676.

75. Huang, Y., Gong, Q., Zhang, Q., Shao, Y., Wang, J., Jiang, Y., ... & Liang, J. (2017). *Nanoscale*, *9*(6), 2340-2347.

76. Wadhwa, R., Agrawal, A. V., & Kumar, M. (2021). *Journal of Physics D: Applied Physics*, *55*(6), 063002.

77. Lee, H. S., Min, S. W., Chang, Y. G., Park, M. K., Nam, T., Kim, H., ... & Im, S. (2012). *Nano letters*, *12*(7), 3695-3700.

78. Piper, J. R., & Fan, S. (2016). *Acs Photonics*, *3*(4), 571-577.

79. Radisavljevic, B., Radenovic, A., Brivio, J., Giacometti, V., & Kis, A. (2011). Single-layer MoS2 transistors. *Nature nanotechnology*, *6*(3), 147-150.

80. Yin, Z., Li, H., Li, H., Jiang, L., Shi, Y., Sun, Y., ... & Zhang, H. (2012). Single-layer MoS2 phototransistors. *ACS nano*, *6*(1), 74-80.

81. Li, S. L., Wakabayashi, K., Xu, Y., Nakaharai, S., Komatsu, K., Li, W. W., ... & Tsukagoshi, K. (2013). Thickness-dependent interfacial coulomb scattering in atomically thin field-effect transistors. *Nano letters*, *13*(8), 3546-3552.

82. Vu, Q. A., Fan, S., Lee, S. H., Joo, M. K., Yu, W. J., & Lee, Y. H. (2018). Near-zero hysteresis and near-ideal subthreshold swing in h-BN encapsulated single-layer MoS2 field-effect transistors. *2D Materials*, *5*(3), 031001.

83. Street, R. A. (2009). *Advanced Materials*, *21*(20), 2007-2022.

84. Xi, Y., Serna, M. I., Cheng, L., Gao, Y., Baniasadi, M., Rodriguez-Davila, R., ... & Minary-Jolandan, M. (2015). *Journal of Materials Chemistry C*, *3*(16), 3842-3847.

85. Gomes, F. O. V., Pokle, A., Marinkovic, M., Balster, T., Anselmann, R., Nicolosi, V., & Wagner, V. (2019). *Solid-State Electronics*, *158*, 75-84.

86. Gao, X., Yin, J., Bian, G., Liu, H. Y., Wang, C. P., Pang, X. X., & Zhu, J. (2021). *Nano Research*, *14*, 2255-2263.

87. Kwack, Y. J., Can, T. T. T., & Choi, W. S. (2021). *npj 2D Materials and Applications*, *5*(1), 84.

88. Cunningham, G., Khan, U., Backes, C., Hanlon, D., McCloskey, D., Donegan, J. F., & Coleman, J. N. (2013). *Journal of Materials Chemistry C*, *1*(41), 6899-6904.

89. Li, J., Naiini, M. M., Vaziri, S., Lemme, M. C., & Östling, M. (2014). *Advanced Functional Materials*, *24*(41), 6524-6531.

90. Lim, Y. R., Song, W., Han, J. K., Lee, Y. B., Kim, S. J., Myung, S., ... & Lim, J. (2016). *Advanced Materials*, *28*(25), 5025-5030.

91. Seo, J. W. T., Zhu, J., Sangwan, V. K., Secor, E. B., Wallace, S. G., & Hersam, M. C. (2019). *ACS applied materials & interfaces*, *11*(6), 5675-5681.

92. Mondal, S. K., Biswas, A., Pradhan, J. R., & Dasgupta, S. (2021). *Small Methods*, *5*(12), 2100634.

93. Michel, M., Desai, J. A., Biswas, C., & Kaul, A. B. (2016). *Nanotechnology*, *27*(48), 485602.

94. Nagashio, K., Yamashita, T., Nishimura, T., Kita, K., & Toriumi, A. (2011). *Journal of Applied Physics*, *110*(2), 024513.

95. Lopez-Sanchez, O., Lembke, D., Kayci, M., Radenovic, A., & Kis, A. (2013). Nature *nanotechnology*, *8*(7), 497-501.

96. Siao, M. D., Shen, W. C., Chen, R. S., Chang, Z. W., Shih, M. C., Chiu, Y. P., & Cheng, C. M. (2018). *Nature communications*, *9*(1), 1442.

97. Lin, Y. J., & Su, T. H. (2017). *Journal of Materials Science: Materials in Electronics*, *28*, 10106-10111.

98. Schmidt, H., Wang, S., Chu, L., Toh, M., Kumar, R., Zhao, W., ... & Eda, G. (2014). *Nano letters*, *14*(4), 1909-1913.

99. Ly, T. H., Perello, D. J., Zhao, J., Deng, Q., Kim, H., Han, G. H., ... & Lee, Y. H. (2016). *Nature communications*, *7*(1), 10426.

100. Yang, M., Kim, T. Y., Lee, T., & Hong, S. (2018). *Scientific reports*, *8*(1), 1-9.

101. Lee, I., Kang, W. T., Kim, J. E., Kim, Y. R., Won, U. Y., Lee, Y. H., & Yu, W. J. (2020). *ACS nano*, *14*(6), 7574-7580.

102. Xiao, S., Xiao, P., Zhang, X., Yan, D., Gu, X., Qin, F., ... & Ostrikov, K. K. (2016). *Scientific reports*, *6*(1), 1-8.

103. Chee, S. S., & Ham, M. H. (2020). *Advanced Materials Interfaces*, *7*(17), 2000762.

104. Kotekar-Patil, D., Deng, J., Wong, S. L., Lau, C. S., & Goh, K. E. J. (2019). *Applied Physics Letters*, *114*(1), 013508.

105. Xie, J., Patoary, N. M., Zhou, G., Sayyad, M. Y., Tongay, S., & Esqueda, I. S. (2022). *Nanotechnology*, *33*(22), 225702.

106. Late, D. J., Liu, B., Matte, H. R., Dravid, V. P., & Rao, C. N. R. (2012). *ACS nano*, *6*(6), 5635-5641.

107. Ahn, J. H., Parkin, W. M., Naylor, C. H., Johnson, A. C., & Drndić, M. (2017). *Scientific reports*, *7*(1), 4075.

108. Amani, M., Chin, M. L., Birdwell, A. G., O'Regan, T. P., Najmaei, S., Liu, Z., ... & Dubey, M. (2013). *Applied Physics Letters*, *102*(19).

109. Tan, D., Jiang, C., Li, Q., Bi, S., & Song, J. (2020). *Journal of Materials Science: Materials in Electronics*, *31*, 15669-15696.

110. Ahn, Y., Jeong, Y., & Lee, Y. (2012). *ACS applied materials & Interfaces*, *4*(12), 6410-6414.

111. Scardaci, V., Coull, R., Lyons, P. E., Rickard, D., & Coleman, J. N. (2011). *Small*, *7*(18), 2621-2628.

112. L. Hu, H. S. Kim, J.-Y. Lee, P. Peumans, Y. Cui, *ACS Nano* **2010**, *4*, 2955.

113. Myja, H., Yang, Z., Goldthorpe, I. A., Jones, A., Musselman, K. P., Grundmann, A., ... & Bacher, G. (2023). *Nanotechnology*.

114. Atkinson, J., & Goldthorpe, I. A. (2020). *Nanotechnology*, *31*(36), 365201.

115. Sannicolo, T., Charvin, N., Flandin, L., Kraus, S., Papanastasiou, D. T., Celle, C., ... & Bellet, D. (2018). *ACS nano*, *12*(5), 4648-4659.

116. Saw, M. J., Ghosh, B., Nguyen, M. T., Jirasattayaporn, K., Kheawhom, S., Shirahata, N., & Yonezawa, T. (2019). *ACS omega*, *4*(8), 13303-13308.

117. Triyana, K., & Suharyadi, E. (2017, May). *IOP Conference Series: Materials Science and Engineering* (Vol. 202, No. 1, p. 012055). IOP Publishing.

118. Tomiyama, T., Mukai, I., Yamazaki, H., & Takeda, Y. (2020). *Optical Materials Express*, *10*(12), 3202-3214.

119. Liu, M., Liao, J., Liu, Y., Li, L., Wen, R., Hou, T., ... & Hao, Y. (2023). *Advanced Functional Materials*, 2212773.

120. Cohen, A., Patsha, A., Mohapatra, P. K., Kazes, M., Ranganathan, K., Houben, L., ... & Ismach, A. (2020). *ACS nano*, *15*(1), 526-538.

121. Zhou, M., Wang, W., Lu, J., & Ni, Z. (2021). *Nano Research*, *14*, 29-39.

122. Li, L., & Carter, E. A. (2019). *Journal of the American Chemical Society*, *141*(26), 10451-10461.

123. Andrzejewski, D., Myja, H., Heuken, M., Grundmann, A., Kalisch, H., Vescan, A., ... & Bacher, G. (2019). *ACS Photonics*, *6*(8), 1832-1839.

124. Lien, D. H., Uddin, S. Z., Yeh, M., Amani, M., Kim, H., Ager III, J. W., ... & Javey, A. (2019). *Science*, *364*(6439), 468-471.

125. Deignan, G., & Goldthorpe, I. A. (2017). *RSC advances*, *7*(57), 35590-35597.

126. Madeira, A., Plissonneau, M., Servant, L., Goldthorpe, I. A., & Tréguer-Delapierre, M. (2019). *Nanomaterials*, *9*(6), 899.

127. Li, F. W., Yen, T. C., Manavalan, S., & Liou, G. S. (2021). *ACS Applied Polymer Materials*, *3*(6), 2971-2978.

128. Lee, J. C., Min, J., Jesuraj, P. J., Hafeez, H., Kim, D. H., Lee, W. H., ... & Ryu, S. Y. (2019). *Microelectronic Engineering*, *206*, 6-11.

129. Ma, C., Gao, X. M., Bi, Y. G., Zhang, X. L., Yin, D., Wen, X. M., ... & Sun, H. B. (2020). *Organic Electronics*, *84*, 105727.

130. Khan, A., Nguyen, V. H., Muñoz-Rojas, D., Aghazadehchors, S., Jiménez, C., Nguyen, N. D., & Bellet, D. (2018). *ACS applied materials & Interfaces*, *10*(22), 19208-19217.

131. Aghazadehchors, S., Nguyen, V. H., Munoz-Rojas, D., Jiménez, C., Rapenne, L., Nguyen, N. D., & Bellet, D. (2019). *Nanoscale*, *11*(42), 19969-19979.

132. Lee, D. G., Lee, D., Yoo, J. S., Lee, S., & Jung, H. S. (2016). *Nano Convergence*, *3*, 1-7.

133. Huang, Y., Wu, J., Xu, X., Ho, Y., Ni, G., Zou, Q., ... & Özyilmaz, B. (2013). *Nano Research*, *6*(3), 200-207.

134. Ippolito, S., Kelly, A. G., Furlan de Oliveira, R., Stoeckel, M. A., Iglesias, D., Roy, A., ... & Samori, P. (2021). *Nature Nanotechnology*, *16*(5), 592-598.

135. Atkinson, J. (2023). Silver Nanowire Networks in Electrochromic Devices. *UWSpace*. http://hdl.handle.net/10012/19488

136. Cho, S., Kang, S., Pandya, A., Shanker, R., Khan, Z., Lee, Y., ... & Ko, H. (2017). *ACS nano*, *11*(4), 4346-4357.